European Journal of Mechanics / B Fluids 94 (2022) 171–189

Contents lists available at ScienceDirect

European Journal of Mechanics / B Fluids

journal homepage: www.elsevier.com/locate/ejmflu

MPS–FEM coupled method for 3D dam-break flows with elastic gate structures

Guanyu Zhang [a], Ruosi Zha [b], Decheng Wan [a,*]

[a] Computational Marine Hydrodynamics Lab (CMHL), School of Naval Architecture, Ocean and Civil Engineering, Shanghai Jiao Tong University, Shanghai 200240, China
[b] School of Ocean Engineering and Technology, Sun Yat-sen University, Zhuhai 519082, China

ARTICLE INFO

Article history:
Available online 7 March 2022

Keywords:
Moving Particle Semi-implicit (MPS)
MPS–FEM coupled method
MPSFSI solver
Fluid–structure Interaction (FSI)
Three-dimensional effect

ABSTRACT

In this paper, the MPS–FEM coupled method is applied for the three-dimensional (3D) dam-break flow with elastic gate, where the Moving Particle Semi-implicit (MPS) method and the Finite Element Method (FEM) are respectively used to solve fluid flows and structure deformation. A partitioned coupling strategy of traditional Conventional Serial Staggered (CSS) strategy is employed for MPS method and FEM method coupling. An interfacial data interpolation module called three-dimensional Kernel Function Based Interpolation Technique (3D-KFBI) is developed for the three-dimensional fluid–structure interface. Based on the MPS–FEM coupled method, a self-developed MPSFSI solver is developed. Then, the stability, accuracy, convergence and energy conservation properties of the developed data interpolation algorithm is validated by two cases. Afterwards, the proposed coupled method is applied for the case of dam-break flow interacting with the elastic gate. A good agreement between present numerical result and published experiment data Antoci et al. (2007) demonstrates the accuracy and efficiency of the present coupled method. At last, MPSFSI solver is applied for the problem of the narrow dam-break flow with the elastic gate to investigate the three-dimensional effect.

1. Introduction

Fluid–structure Interaction (FSI) phenomena are frequently observed in hydrodynamics and ocean engineering. For instance, hydrodynamic slamming on marine vessels, tsunami impact on offshore structures, sloshing in liquid containers and so on. Such phenomena, usually accompanied by tremendous hydrodynamic loads acting on the structure, may cause considerable structural deformation and even have severe challenges to the structural safety. Therefore, taken the structure response during hydrodynamic analysis into consideration is of substantial importance for the precise evaluations and reliable designs of offshore and ocean structures.

The main characteristics of FSI phenomena in the field of ocean engineering can be summarized as violent free surface flows, strong nonlinear hydrodynamic loads and considerable rigid motions of structures with relatively small responses. Therefore, some special attentions should be paid such as free surface tracking, moving boundary conditions, interfacial treatment and so on. Most of numerical investigations for FSI problems have been performed based on a grid system. The Lagrangian-based Particle Finite Element Method (PFEM) [1] has been developed for the modeling of FSI problems [2–4]. As a mesh-based method, the PFEM is effective in dealing with free surface tracking, while being quite time-consuming because of the meshes rebuilding. Liao and Hu [5,6] applied Finite Differential Method (FDM) and Finite Element Method (FEM) coupled method to investigate the interaction between surface flow and thin elastic plate, and obtained good results. Paik and Carrica [7] used Chimera (overlapping grid) method for numerical simulation of sloshing flows with deformable baffles. However, the Chimera method requires interpolations between overlapped grids resulting in an accumulated error. Qu et al. [8] analyzed the water entry process of a two-dimensional elastic cylindrical shell by the means of volume of fluid (VOF) and FEM coupled method. The differences of the impact characteristics due to water impact of a rigid body and an elastic body is investigated.

Despite the effectiveness, these grid-based methods may be difficult to adjust and update the grid when coordinating the fluid–solid interface. Therefore, some mesh-free particle methods have aroused a wide attention. Different from the mesh-based method, these mesh-free methods are inherently Lagrangian methods, by which a continuum system is discretized into moving particles. In addition, the meshfree particle methods avert the treatment of mesh rebuilding or the capture of free surface. Thus, meshfree particle methods can deal with the large deformation and strong nonlinear phenomenon of free surfaces

* Corresponding author.
E-mail address: dcwan@sjtu.edu.cn (D. Wan).

https://doi.org/10.1016/j.euromechflu.2022.02.014
0997-7546/

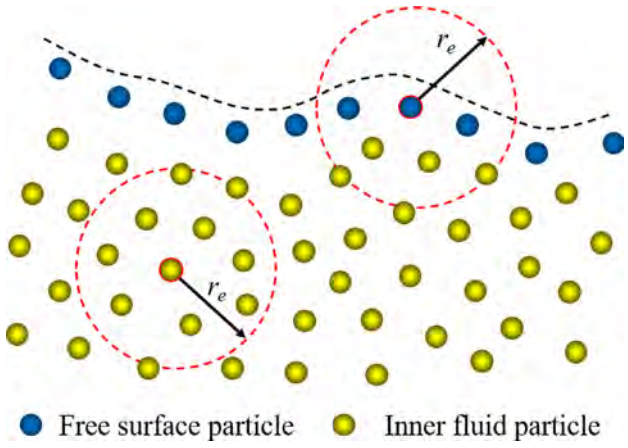

Fig. 1. Sketch of free-surface detection.

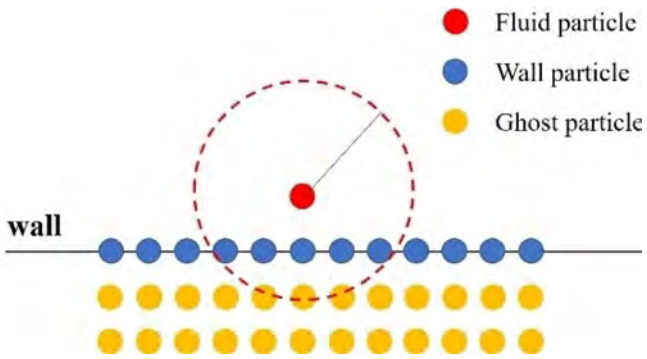

Fig. 2. Schematic of boundary particles.

relative easier, as well as the moving boundaries. Over past decades, particle-based methods have been intensely studied, such as the Smoothed Particle Hydrodynamics (SPH) [9], the Moving Particle Semi-implicit (MPS) Method [10], and many others. Up until now, numerous good works employing particle-based methods are carried out to study violent FSI problems, for instance, the dam-break wave [11–13], the water entry [14–16], the liquid sloshing [17–20], the wave–ship interaction [21–25], multiphase flow problem [26–28] and so on. All of the above studies presented highly performance in capturing the violent free surface flows and accurately predicting the impacting force. Simultaneously, some studies of particle methods have focused on the structural dynamic response in FSI problems. Fully-Lagrangian coupling methods have been proposed to analyze FSI problems [29]. Antoci et al. [30] performed simulations of dam-break flow interacting with an elastic gate by SPH method. Liu et al. [31] applied SPH method in hydro-elastic problems, where the fluid particles were used to model the free surface flows governed by Navier–Stokes equations and the solid particles were used to model the elastic solid objects. Hwang et al. [32,33] developed the MPS-based FSI analysis method for simulations of sloshing flow with a deformable baffle. Yang and Zhang [34] developed modified MPS method with large eddy simulation (LES) model to study FSI problems. Khayyer et al. [35] presented enhanced ISPH–SPH coupled method for simulating incompressible FSI benchmarks. Falahaty et al. [36] developed enhanced MPS-based method in FSI modeling, where the stress point integration was incorporated in calculation of structural dynamics. Khayyer et al. [37] proposed a multi-resolution MPS method for incompressible fluid–elastic structure interactions. Lyu et al. [38] applied Total Lagrangian SPH (TLSPH) method in 2D FSI problems, and the tensile instability problem is suppressed through Tensile Instability Control (TIC) and Particle Shifting Technique (PST). For the 3D simulations of FSI problems, Khayyer et al. [39] presented the first 3D entirely Lagrangian meshfree projection-based hydroelastic FSI solver and validated the solver through sets of rigorous test cases. Sun et al. [40] presented TLSPH method to investigate the 3D effects in the FSI dam-breaking and sloshing cases. Yilmaz et al. [41] developed rigid multibody system and WCSPH method coupling model, the present model is validated through benchmark cases of 3D dam-break flow impacting on the deformable elastic boundaries. Many researchers also have taken advantage of the Lagrangian particle methods along with other robust structure computational method to develop coupled FSI solvers. Sun et al. [42,43] performed coupled MPS-modal superposition method for 2D and 3D fluid–structure interaction problems with free surface. Because of the accuracy of FEM in solving structural dynamics, many researches kept the focus on studying FSI problems based on particle method coupled with FEM. Lee et al. [44], Mitsume et al. [45,46], Zheng et al. [47,48] and Zhang et al. [49] successfully simulated fluid–elastic structure interactions through the coupled MPS–FEM method. Fourey et al. [50,51], Yang et al. [52], Hermange et al. [53] and Zhang et al. [54] applied SPH–FEM coupled method in FSI problems. Mitsume et al. [45] adopted MPS–FEM coupling method, in which the boundary particles overlapped with the finite element grid, and information was exchanged at the fluid–structure interface based on linear interpolation technology. Fourey et al. [51] adopted the pressure integral average method for the process of fluid–structure interface interpolation in SPF–FEM method. Zheng et al. [47] used explicit MPS method and FEM coupling method to simulate FSI problems. In the coupling algorithm, the elements for structural discretization in FEM can straightforwardly serve as boundary ghost cells for interaction force calculation in MPS. In the process of fluid–structure interface interpolation, the integral version of MPS method can be used to calculate the force at integration points of cells are distributed to the structure nodes to update the structural boundary.

However, above mentioned literatures are almost concentrating on 2D FSI problems. The main challenges of 3D simulations of FSI problems are complicate interface treatment between fluid and structure field, large computing and so on. In recent years, some studies have obtained noticeable achievements on simulations of 3D FSI problems. Zhang and Wan [55] developed a 3D MPS–FEM coupled method for simulating 3D liquid sloshing in an elastic tank, an 2D interfacial data interpolation algorithm was proposed to couple particle model and element model. Hermange et al. [56] proposed the 3D SPH–FEM coupled method for the application to complex tire hydroplaning simulations on rough ground. A Conventional Parallel Staggered (CPS) procedure was applied for coupling two methods. Lee and Hong [57] applied a 3D SPH–FEM coupled method for the accurate estimation of the dam-break flow impacting on an elastic column, the optimizations of the Equation of State (EOS) and some simulation parameters such as the time step and initial particle spacing were considered. Zheng et al. [48] developed a 3D explicit MPS–FEM coupling algorithm. The solid boundary was modeled by ghost cell boundary (GCB) model, which has proved to be an effective method to deal with wall boundaries of complicated shapes. In this work, a 3D MPS–FEM coupled method is developed to investigate FSI problems, where the MPS method is applied for solving the fluid domain and the FEM is used to solve the structure responses. In our previous study [49], two weight function interpolation techniques based on shape function and kernel function, called Shape Function Based Interpolation Technique (SFBI) and Kernel Function Based Interpolation Technique (KFBI)

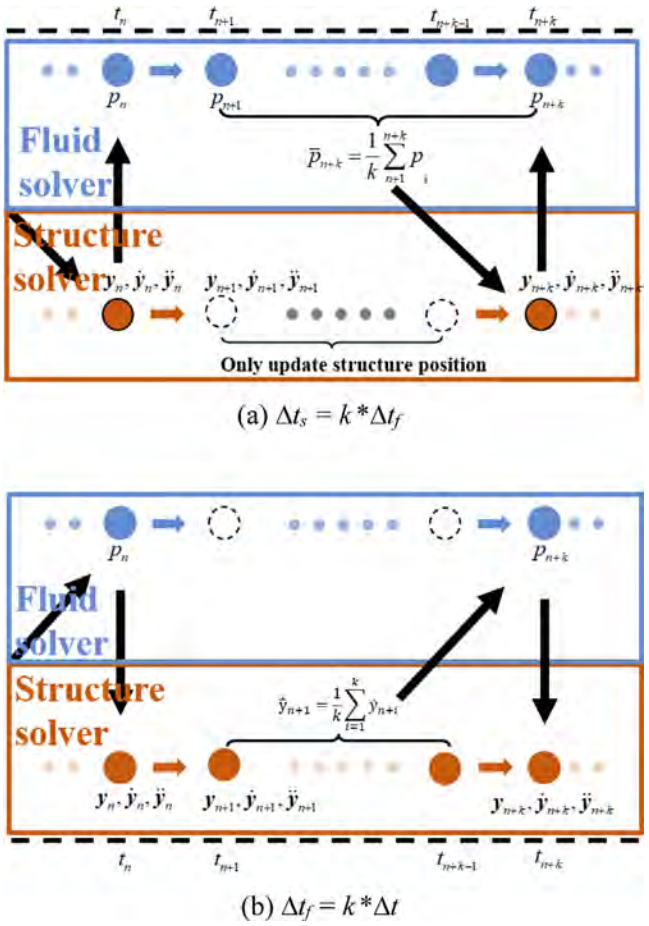

Fig. 3. Schematic diagram of partitioned coupling strategy between fluid and structure field.

were introduced to achieve the data exchange on the 2D isomerous fluid–structure interface. In this paper, KFBI for the 3D isomerous interface is developed to simulate the 3D FSI problems.

In this paper, a 3D MPS–FEM coupled method is developed for the 3D free surface flow with deformable structures. To couple MPS method and FEM method, a partitioned coupling strategy of traditional Conventional Serial Staggered (CSS) strategy is employed. To realize the interpolation process on the space–time isomerous fluid–structure interface, the different time steps are adopted in both field and an interpolation technique of 3D-KFBI is developed for the data exchange. Based on the MPS–FEM coupled method, a self-developed MPSFSI solver is developed. The present paper is organized as follows: Section 2 introduces the theories of the MPS and the FEM methods. The coupling scheme and interpolation technique at the interface between fluid and structure field are introduced in Section 3. Then, the accuracy of interpolation module is validated through two benchmarks. The performance of 3D MPS–FEM coupled solver is validated in Section 4 through a FSI benchmark of dam-break flow with an elastic gate. The comparisons between the present numerical result and experimental data [30] are conducted. Finally, to study the 3D effects, the simulation of narrow dam-break flow with an elastic gate is carried out.

2. Numerical method

In this study, the partitioned MPS–FEM method is adopted to investigate the FSI problems. The MPS method is used to calculate the fluid field, while the FEM is adopted to solve the structure field. The theories for the MPS have been presented with details in our previous papers [55,58–64].

2.1. MPS formulation for fluid dynamics

2.1.1. Governing equations

In the MPS method, the governing equations for the fluid particles mainly include the continuity equations and momentum equation. The Navier–Stokes equations are expressed in Lagrangian form as following,

$$\nabla \cdot \boldsymbol{V} = 0 \tag{1}$$

$$\frac{D\boldsymbol{V}}{Dt} = -\frac{1}{\rho}\nabla P + \nu\nabla^2\boldsymbol{V} + \boldsymbol{g} \tag{2}$$

where ρ and ν denote the fluid density and kinematic viscosity, $\boldsymbol{V}$, P and $\boldsymbol{g}$ present the velocity vector, the pressure and the gravitational acceleration. In the MPS method, the physical quantities of particles are expressed based on the Lagrangian formulation, and therefore the calculation of convection term is not required.

2.1.2. Kernel function

In the MPS method, governing equations should be expressed by the particle interaction models based on the kernel function. The kernel function in present paper can be formulated as,

$$W(r) = \begin{cases} \dfrac{r_e}{0.85r + 0.15r_e} - 1 & 0 \le r < r_e \\ 0 & r_e \le r \end{cases} \tag{3}$$

where r is the distance between two particles, r_e denotes the influence radius of the target particle. The adopted kernel function can avoid the non-physical pressure oscillation, and improve the computational stability. The value of r_e is distinct in different particle interaction models.

2.1.3. Particle interaction models

Models of particle interaction include gradient model, divergence model and Laplacian model. These models can be written as,

$$\langle\nabla\phi\rangle_i = \frac{D}{n^0}\sum_{j\neq i}\frac{\phi_j + \phi_i}{\left|\boldsymbol{r}_j - \boldsymbol{r}_i\right|^2}(\boldsymbol{r}_j - \boldsymbol{r}_i)\cdot W(\left|\boldsymbol{r}_j - \boldsymbol{r}_i\right|) \tag{4}$$

$$\langle\nabla\cdot\boldsymbol{\Phi}\rangle_i = \frac{D}{n^0}\sum_{j\neq i}\frac{\left(\boldsymbol{\Phi}_j - \boldsymbol{\Phi}_i\right)\cdot(\boldsymbol{r}_j - \boldsymbol{r}_i)}{\left|\boldsymbol{r}_j - \boldsymbol{r}_i\right|^2}W(\left|\boldsymbol{r}_j - \boldsymbol{r}_i\right|) \tag{5}$$

$$\left\langle\nabla^2\phi\right\rangle_i = \frac{2D}{n^0\lambda}\sum_{j\neq i}\left(\phi_j - \phi_i\right)\cdot W(\left|\boldsymbol{r}_j - \boldsymbol{r}_i\right|) \tag{6}$$

$$\lambda = \frac{\sum_{j\neq i} W\left(\left|\boldsymbol{r}_j - \boldsymbol{r}_i\right|\right)\left|\boldsymbol{r}_j - \boldsymbol{r}_i\right|^2}{\sum_{j\neq i} W\left(\left|\boldsymbol{r}_j - \boldsymbol{r}_i\right|\right)} \tag{7}$$

where ϕ is a scalar function, $\boldsymbol{\Phi}$ presents a vector, D is the number of space dimensions, r is the position vector, λ is a parameter and expressed as Eq. (7), and n^0 is the initial density of the particle number. Koshizuka [11] proposed the value of r_e in each particle interaction model through a series of numerical tests, as shown in Table 1, where l_0 is the initial spacing of particles.

2.1.4. Pressure Poisson Equation

The pressure is calculated by solving the Pressure Poisson Equation (PPE). A mixed source term method, proposed by Tanaka and Masunaga [65] and Lee et al. [66], is applied in the present

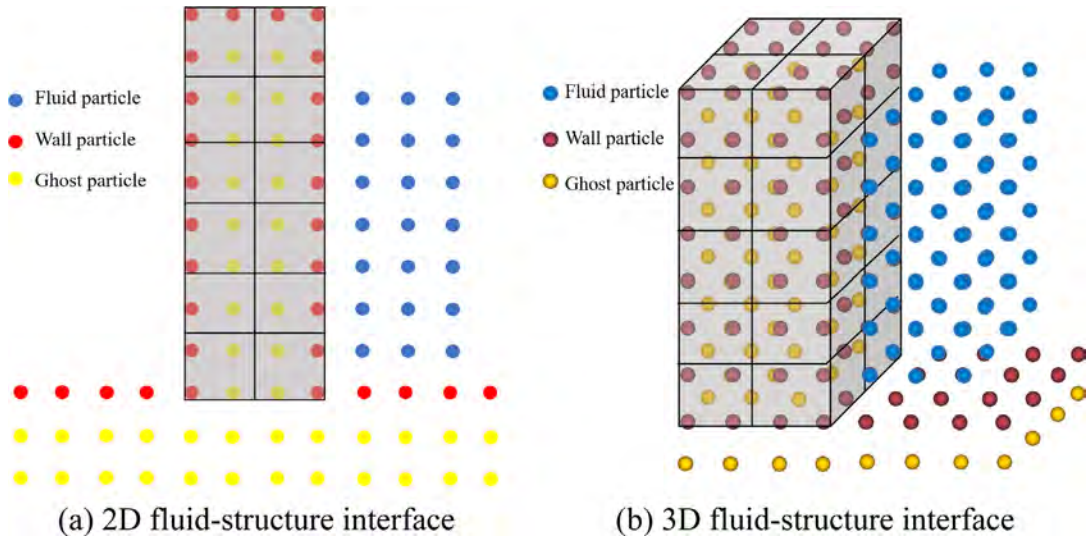

Fig. 4. The schematic diagram of the 2D and 3D fluid–structure interface.

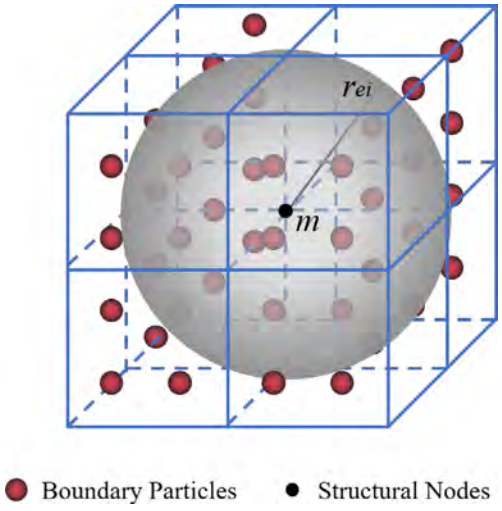

Fig. 5. The schematic diagram of the force interpolation.

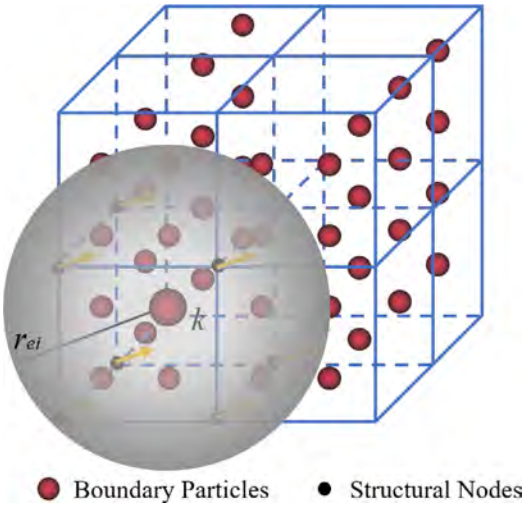

Fig. 6. The schematic diagram of the displacement interpolation.

Table 1
The values of r_e in different particle interaction models.

Particle interaction model	r_e
Gradient model	$r_{e\_gra} = 2.1 * l_0$
Divergence model	$r_{e\_div} = 2.1 * l_0$
Laplacian model	$r_{e\_lap} = 4.01 * l_0$

solver, which combines the velocity divergence-free condition and constant particle number density condition.

$$\left\langle \nabla^2 p^{k+1} \right\rangle_i = (1-\gamma)\frac{\rho}{\Delta t}\nabla \cdot V_i^* - \gamma \frac{\rho}{\Delta t^2}\frac{\langle n^k \rangle_i - n^0}{n^0} \tag{8}$$

where P_{k+1}, Δt and V_i^* are the pressure of the step $k+1$, time step and temporal velocity. γ is the weight of the particle number density term between 0 to 1. The range of $0.01 \leq \gamma \leq 0.05$ is better according to numerical experiments conducted by Lee et al. [66]. In this paper, $\gamma = 0.01$ is adopted throughout all simulations. n^k is the temporal particle number density and defined as,

$$\langle n^k \rangle_i = \sum_{j \neq i} W(|\boldsymbol{r}_j - \boldsymbol{r}_i|) \tag{9}$$

2.1.5. Free surface detection

Surface particles need to be detected to impose Dirichlet boundary conditions on the pressure Poisson equation, and is essential in accurately imposing boundary effects. In general, the particle number density can be regarded as a means of detecting free surface particles. When the particle number density satisfies the expression,

$$(\langle n \rangle_i / n^0) < \beta \tag{10}$$

where β is a parameter with a value of 0.8 in this paper, the particle will be determined as a free surface particle. When $(\langle n \rangle_i / n^0) > 0.97$, the particle is regarded as an internal particle. Otherwise, if $0.8 < (\langle n \rangle_i / n^0) < 0.97$, an improved surface particle detection method [67] based on the asymmetry arrangement of neighboring particles, as shown in Fig. 1, is applied,

$$\langle \boldsymbol{F} \rangle_i = \frac{D}{n^0}\sum_{j \neq i}\frac{(\boldsymbol{r}_j - \boldsymbol{r}_i)}{|\boldsymbol{r}_j - \boldsymbol{r}_i|} W(|\boldsymbol{r}_j - \boldsymbol{r}_i|) \tag{11}$$

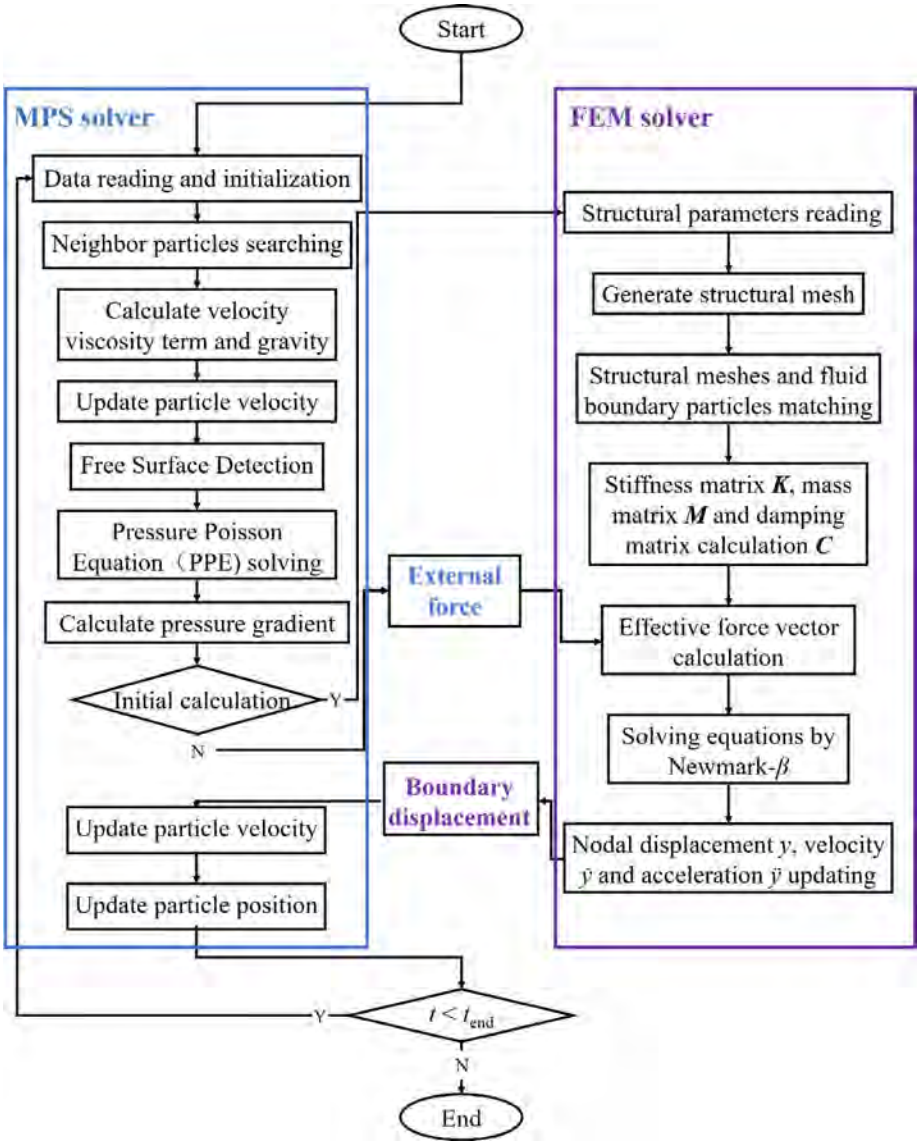

Fig. 7. The flowchart of the MPS–FEM coupled method.

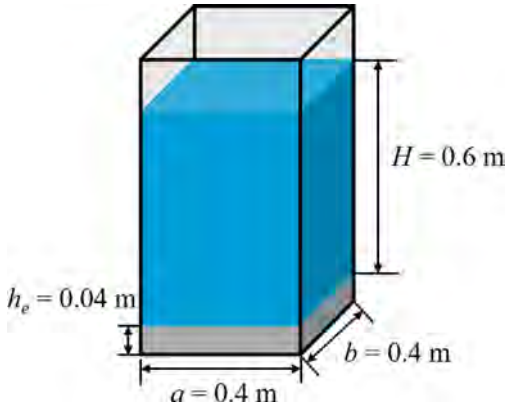

Fig. 8. Schematic sketch of hydrostatic water column on a deformable plate.

where $\boldsymbol{F}$ represents the asymmetric arrangements of neighbor particles. Particles satisfying $\langle|\boldsymbol{F}|\rangle_i > \alpha\,|\boldsymbol{F}|^0$ will be regarded as free surface particles, where α is a parameter with a value of 0.9 in this paper, $|\boldsymbol{F}|^0$ is the initial value of $|\boldsymbol{F}|$ for surface particles.

2.1.6. Boundary condition

In the MPS method, the boundary condition of free surface is accomplished when the zero pressure is imposed to the free surface particles. For the solid boundary, the arrangement of multilayer particles, as shown in Fig. 2, comprises one layer of wall particles and two layers of ghost particles. The arrangement of ghost particles is to fulfill the particle number density so that the particle interaction can be properly calculated near the solid boundary. The calculation of wall particles' pressures is the same as fluid particles, solving by PPE. While the pressures of ghost particles are obtained by interpolation. The advantage of present arrangement is that it can ensure a smooth and accurate pressure field around the solid surface and prevent fluid particles from penetrating into the impermeable boundary.

2.2. FEM formulation for structure dynamics

In this paper, the 3D FEM method with hexahedral solid element is applied for the structural analysis. According to the

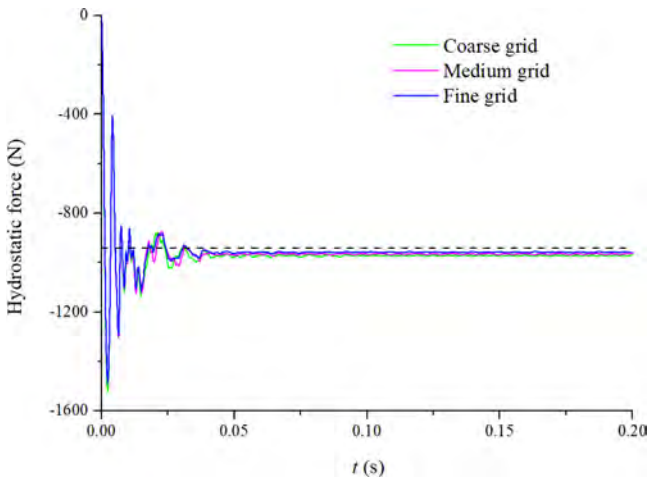

Fig. 9. The time history of hydrostatic force subjected to the plate.

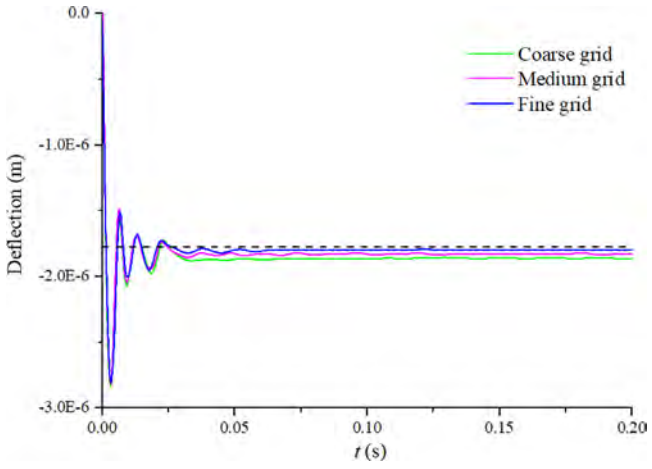

Fig. 10. The time histories of deflection at the plate's center point.

theory of FEM, after the structure is discretized, the dynamic balance equation of nodes can be written as follows:

$$\mathbf{M}\ddot{\boldsymbol{y}} + \mathbf{C}\dot{\boldsymbol{y}} + \mathbf{K}\boldsymbol{y} = \boldsymbol{F} \tag{12}$$

$$\mathbf{C} = \beta_1\mathbf{M} + \beta_2\mathbf{K} \tag{13}$$

where **M**, **C** and **K** represent the mass, damping and stiffness matrices of the structure analysis. $\boldsymbol{F}$ is the force vector of the structure and varies with computational time. For simplicity of implementation, the Rayleigh damping is used, damping matrix **C** is assumed to be a linear combination of **M** and **K**, where β_1 and β_2 are the Rayleigh damping coefficients. According to Newmark [68], the structural node displacement at $t = t + \Delta t$ can be solved with the help of Taylor's expansions of velocity and displacement:

$$\dot{y}_{t+\Delta t} = \dot{y}_t + (1-\gamma)\ddot{y}_t\Delta t + \gamma\ddot{y}_{t+\Delta t}\Delta t, 0 < \gamma < 1 \tag{14}$$

$$y_{t+\Delta t} = y_t + \dot{y}_t\Delta t + \frac{1-2\beta}{2}\ddot{y}_t\Delta t^2 + \beta\ddot{y}_{t+\Delta t}\Delta t^2, 0 < \beta < 1 \tag{15}$$

where β and γ are parameters in the Newmark-β method and set as $\beta = 0.25$, $\gamma = 0.5$ for all simulations. The nodal displacements at $t = t + \Delta t$ can be solved by the following formula [69]:

$$\overline{\mathbf{K}}\mathbf{y}_{t+\Delta t} = \overline{\boldsymbol{F}}_{t+\Delta t} \tag{16}$$

$$\overline{\mathbf{K}} = \mathbf{K} + a_0\mathbf{M} + a_1\mathbf{C} \tag{17}$$

$$\overline{\boldsymbol{F}}_{t+\Delta t} = \boldsymbol{F}_t + \mathbf{M}(a_0 y_t + a_2\dot{y}_t + a_3\ddot{y}_t) + \mathbf{C}(a_1 y_t + a_4\dot{y}_t + a_5\ddot{y}_t) \tag{18}$$

$$a_0 = \frac{1}{\beta\Delta t^2}, a_1 = \frac{\gamma}{\beta\Delta t}, a_2 = \frac{1}{\beta\Delta t}, a_3 = \frac{1}{2\beta} - 1,$$
$$a_4 = \frac{\gamma}{\beta} - 1, a_5 = \frac{\Delta t}{2}\left(\frac{\gamma}{\beta} - 2\right), a_6 = \Delta t\,(1-\gamma)\,, a_7 = \gamma\,\Delta t \tag{19}$$

where $\overline{\mathbf{K}}$ and $\overline{\boldsymbol{F}}$ are referred to as effective stiffness matrix and effective force vector, respectively. In 3D solid element, the effective stiffness matrix is a large-scale symmetric sparse matrix. In present paper, we propose a compressed sparse row (CSR) format based BiCGSTAB algorithm for solving above system of linear algebraic equations.

2.3. Determination of time step

The time-step Δt_f for MPS method will fulfill the Courant–Friedrichs–Lewy (CFL) condition, given by the following formula,

$$\Delta t_f \leq \frac{Cl_0}{u_{max}} \tag{20}$$

where C is the Courant number between 0 to 1, u_{max} is the maximum instantaneous velocity of particles. In the FEM solver, the time-step Δt_s is determined based on the central difference method, defined by,

$$\Delta t_s \leq \frac{L_{min}}{C_s} \tag{21}$$

where L_{min} represents the minimum size of grid, C_s denotes the velocity of elastic wave and can be defined as,

$$C_s = \sqrt{\frac{E_s(1-\mu_s)}{\rho_s(1+\mu_s)(1-2\mu_s)}} \tag{22}$$

where E_s, μ_s and ρ_s denote the Young's modulus, Poisson's ratio, and density of structure, respectively. To ensure numerical stability, the time-step Δt, employed in FSI solver needs to satisfy the following formula,

$$\Delta t \leq \min\left\{\Delta t_f, \Delta t_s\right\} \tag{23}$$

For the conducted test cases of this study, since relatively flexible structures were considered, the time-step for MPS method was smaller than that of the FEM method. However, according to Eq. (21), for stiff structures with large velocity of elastic wave, the time step of structure domain would become smaller than that of the fluid domain. Proper set up of the calculation time step for fluid and structure would be important to maintain computational stability and at the same time conduct efficient calculations.

3. MPS-FEM coupled scheme

A partitioned 3D MPS–FEM coupled method is applied in this work to simulate FSI problems. The coupling algorithm and implementation strategy of the whole process will be introduced in this section, as well as the validation of the interface data transformation.

3.1. Coupling algorithm between the MPS and FEM method

In the coupling algorithm, the MPS method is used for solving fluid flow, while the FEM is applied for the structural dynamics. The proposed MPS–FEM coupled method combines both advantages of MPS and FEM, consisting of the convenience of MPS in simulating free-surface fluid dynamics and the accuracy of FEM in

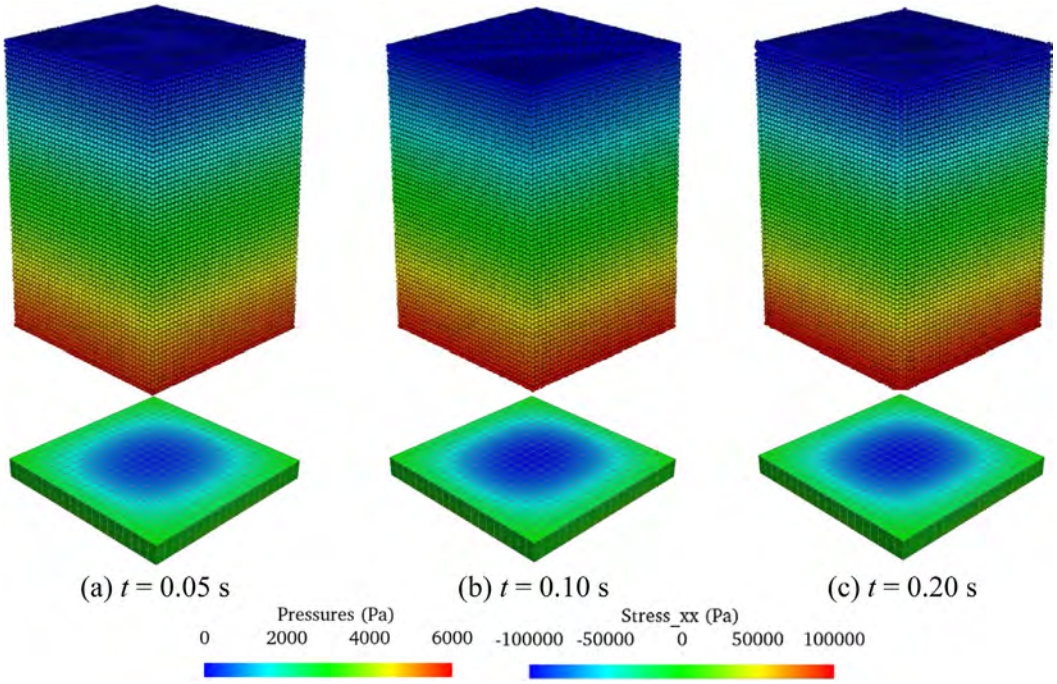

Fig. 11. A hydrostatic water column on a deformable plate, typical snapshots of the pressure/stress distribution on particle model.

solving structural dynamics. The traditional Conventional Serial Staggered (CSS) strategy is employed for coupling the MPS and FEM method, as shown in Fig. 3. The time step sizes for fluid analysis and structure analysis are set as Δt_f and Δt_s. It is notable that the fluid domain and structure field are discretized by different time steps to satisfy the stability of both computation domains. When the time step of structure domain Δt_s is larger than Δt_f, $\Delta t_s = k * \Delta t_f$ is applied, where k is an integer. The coupling strategy is shown in Fig. 3(a). In each cycle of FSI simulation, the fluid domain is performed based on the MPS method from the time step t_{n+1} to t_{n+k}. Mean pressures $\overline{p}_{n+k}$ of particles on the fluid–structure interface are calculated. Then, external force acting on the structure node is calculated based on the average pressure $\overline{p}_{n+k}$ at the time step t_{n+k}. The position and velocity of boundary particles are updated and considered as new boundary conditions for the calculation of fluid domain at next time step. It should be noted that the position of boundary particles will be updated within the time steps t_{n+1} and t_{n+k-1} based on velocity of particles calculated at t_n to avoid the instability of fluid field produced by the large displacements of boundary particles within Δts. In contrast, if Δt_s is smaller, $\Delta t_f = k * \Delta t_s$ is applied. The coupling strategy is shown in Fig. 3(b). It can indicate that present strategy is utility for its advantages of flexibility and convenient realization.

Similar to the 2D fluid–structure interface, the 3D fluid–structure interface is shown in Fig. 4(b). An interface interpolation algorithm with certain precision is employed in the proposed coupling method to satisfy the interface condition of displacement and traction equilibrium and denoted as,

$$\boldsymbol{u}^F = \boldsymbol{u}^S \tag{24}$$

$$p^F \boldsymbol{n}^F = -p^S \boldsymbol{n}^S \tag{25}$$

where $\boldsymbol{n}^S$ and $\boldsymbol{n}^F$ are normal vectors to structure and fluid interface particles. The superscript F and S represent the physical quantities in the fluid solver and structure solver, respectively. Then, the 3D Kernel Function Based Interpolation Technique (3D-KFBI) is proposed for the data interpolation, including the force transformation and the deformation transformation.

The schematic diagram of the 3D-KFBI technique for the force transformation from the fluid domain to the structural field is demonstrated in Fig. 5. For structure node m, the boundary particle of the fluid domain will be denoted as a neighbor particle of structure node while the distance between the boundary particle and structure node is smaller than the interpolation effective radius r_{ei} of interpolation. In this paper, according to previous research [49], the value of effective radius r_{ei} is set as $0.5 * r_{e\_gra}$, which is slightly larger than l_0. The weighted value of the fluid force of the neighbor particle $W(|\boldsymbol{r}_i - \boldsymbol{r}_m|)$ is calculated based on Eq. (3). Then, the equivalent nodal hydrodynamic pressure p_m^s corresponding to the node m is estimated by the weighted value of pressure components regarding to the neighbor boundary particles and defined as,

$$p_m^S = \frac{\sum_i p_i \cdot \boldsymbol{n}_i^F \cdot W(|\boldsymbol{r}_i - \boldsymbol{r}_m|)}{\sum_i W(|\boldsymbol{r}_i - \boldsymbol{r}_m|)} \tag{26}$$

The schematic diagram for the deformation transformation of the fluid–structure interface is demonstrated in Fig. 6. The displacement of the boundary particle k is calculated by neighbor nodal displacement when the distance between the structure node and boundary particle k is smaller than the interpolation effective radius r_{ei}. Then boundary particles' displacement $\boldsymbol{w}_k^F$ can be obtained by the interpolation based on the kernel functions $W(|\boldsymbol{r}_i - \boldsymbol{r}_k|)$, and the nodal velocity $\boldsymbol{u}_i$,

$$\boldsymbol{w}_k^F = \frac{\sum_i \boldsymbol{\delta}_i \cdot W(|\boldsymbol{r}_i - \boldsymbol{r}_k|)}{\sum_i W(|\boldsymbol{r}_i - \boldsymbol{r}_k|)} \tag{27}$$

In Fig. 7, the overall flowchart of MPSFSI solver is presented. The fluid solver is executed to obtain the pressure field and transfer the hydrodynamic pressure to structure nodes. With this external force, structural nodal displacement and velocity are obtained through the structural solver. With the known displacements of structural nodes and velocities, the positions of boundary particles can be therefore updated. Due to the different time steps in each solver, the detailed process within each FSI cycle is shown in Fig. 3.

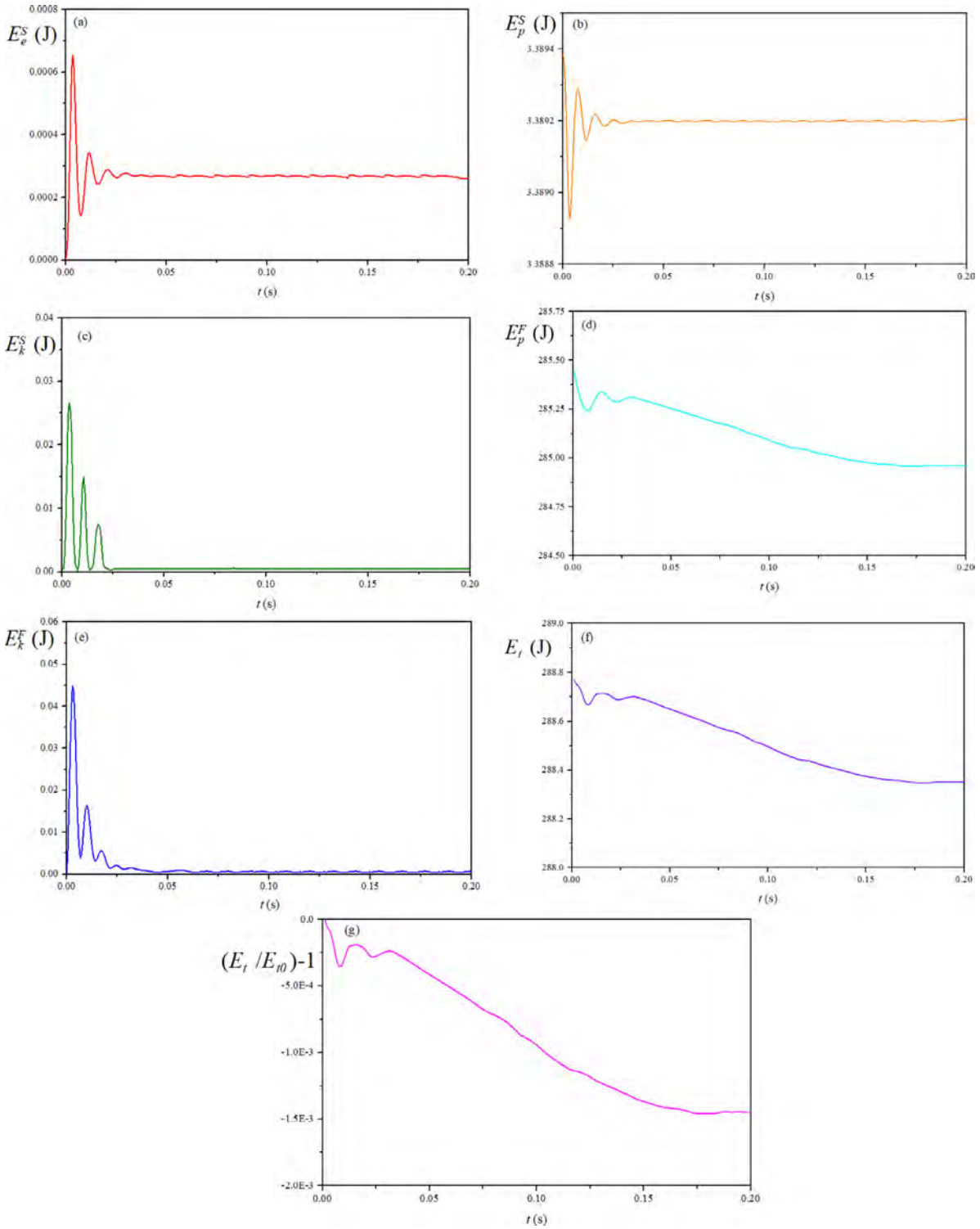

Fig. 12. The time histories of, (a) elastic strain energy of structure, (b) gravitational potential energy of structure, (c) kinetic energy of structure, (d) gravitational potential energy of fluid, (e) kinetic energy of fluid, (f) total energy of FSI system and (g) normalized total energy of the FSI system.

3.2. Validation of interpolation modules

In this section, two benchmarks of 3D hydrostatic water column on a deformable plate and 3D forced deformable plate with the initial velocity are carried out, to validate the coupling algorithm accuracy of the interfacial data transformation including force and deformation. The stability, accuracy, convergence and energy conservation properties of present coupled method can be proved through the above-mentioned tests.

3.2.1. 3D hydrostatic water column on a deformable plate

The first benchmark test is the 3D hydrostatic water column on a deformable plate. Fig. 8 shows a schematic sketch of this benchmark test. The hydrostatic pressure load of a water column of 0.4 m length, 0.4 m width and 0.6 m height is suddenly subjected on an aluminum plate, which eventually reaches an equilibrium state with a constant deformation. The thick (h_e), density (ρ_s), Young's modulus (E_s) and Poisson's ratio (μ_s) of plate are 0.04 m, 2700 kg/m^3, 67.5 GPa and 0.34, respectively, and the

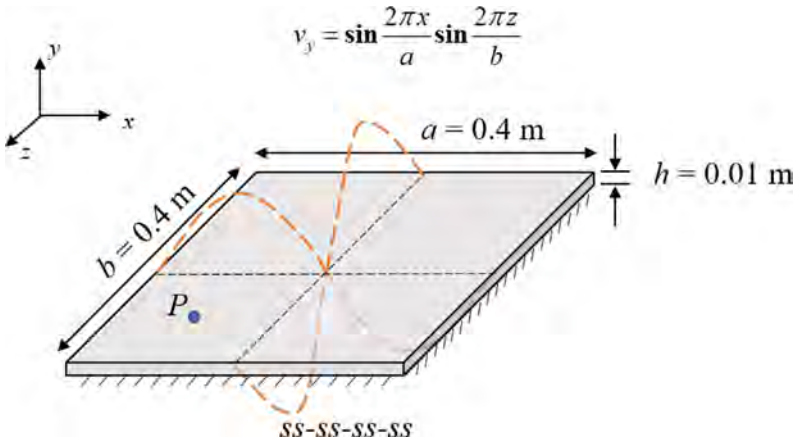

Fig. 13. Schematic illustration of the computational domain for the vibration modes of (2,2).

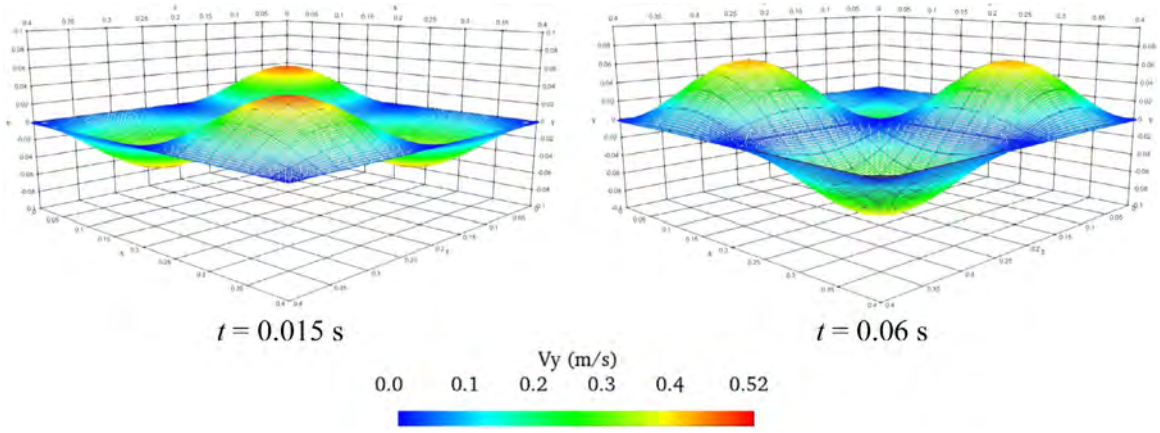

Fig. 14. Coincidence study between the deformed grids and particles.

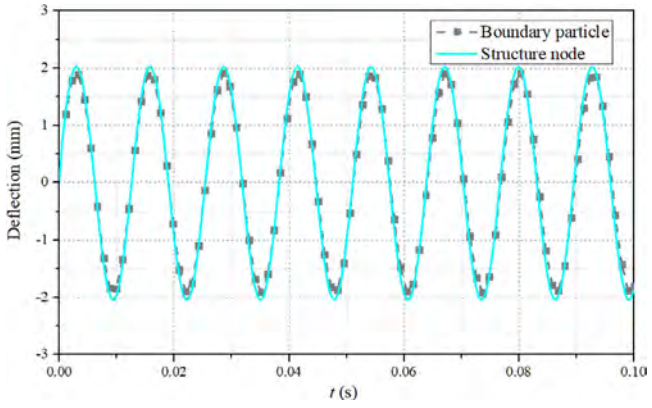

Fig. 15. The time history of the vibration of measuring point.

damping effect is considered during the simulation. The particle spacing is set as 0.008 m, and the time step is regarded as 0.00002 s. The grid convergence studies are conducted in this test, the plate is dispersed into three kinds of grids, maximum grid sizes are set as 0.04 m, 0.02 m and 0.01 m, respectively.

By means of the interfacial data interpolation module, the force on the particle model can be transferred to the nodes of the element model. The time history of hydrostatic force subjected to the plate under different grid discretization is exhibited in Fig. 9. The numerical hydrostatic force will eventually reach a stable status, and the calculated results under different grid discretization are close to the theoretical value. The comparison between the theoretical value and calculated force are shown in Table 2, where F' and F_0 represent the convergent numerical force and theoretical value, respectively. It can be noticed that the calculated results approximate to the theoretical value. The force interpolation module can offer the high accuracy, and have a better grid convergence. According to Ugural [70], the analytic solution of the deflection can be estimated through the load on the plate:

$$w_{max} = w\left(\frac{a}{2}\right) = \alpha\frac{|g|(\rho^F H + \rho^S h_e)a^4}{D} \tag{28}$$

where H corresponds to the height of the water column, and a and D denote the length and the flexural rigidity of plate. α is a parameter depending on boundary support condition together with the ratio of length and width of the plate, the value of α is 0.00406 in this test. Therefore, the magnitude of static deflection at the plate's center point would be $d_0 = -1.773\text{E}{-6}$ m. Fig. 10 shows the time history of the deflection on the center point of the aluminum plate under different grid discretization. The deflection of plate's mid-point will eventually reach a stable status. The accuracy analysis of deflection between the theoretical value and numerical result are shown in Table 3, where d' and d_0 represent the convergent numerical deflection and theoretical value, respectively. The calculated deflections approximate to the theoretical value. It can be proved that the current method can provide accurate estimates of deflection of plate's mid-point.

Fig. 11 presents the pressure and stress fields of the hydrostatic water column on an elastic plate at t = 0.05, 0.1 and 0.2 s

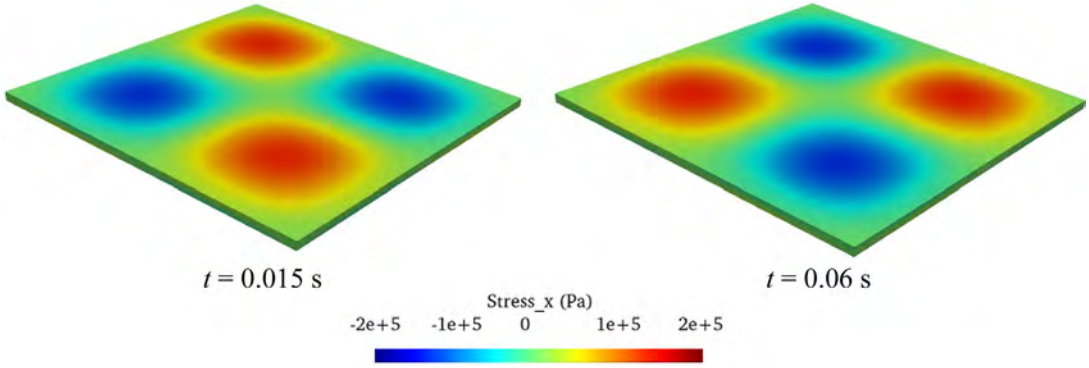

Fig. 16. The stress distribution of deformable structure.

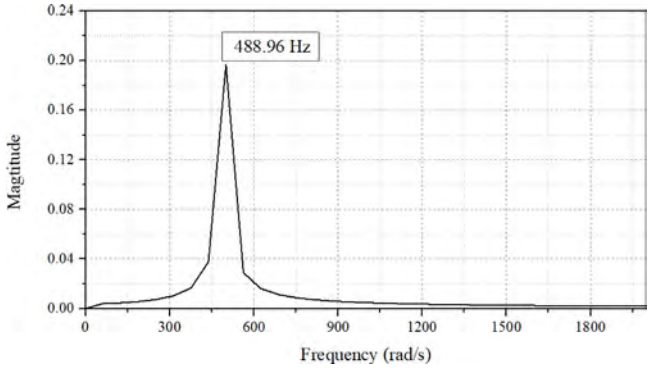

Fig. 17. The frequency of the vibration of measuring point.

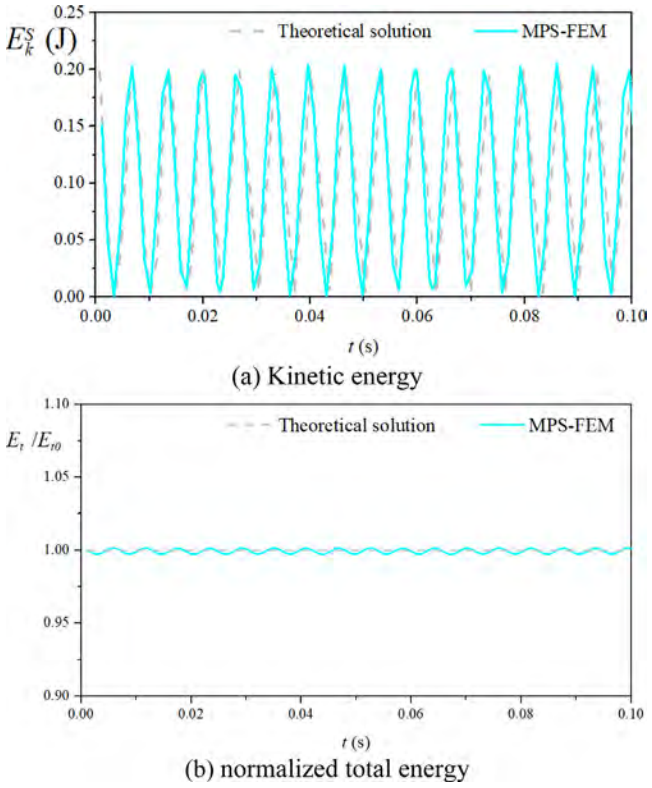

Fig. 18. The time history of kinetic energy and normalized total energy of the plate.

Table 2
The comparisons of hydrostatic loading (N) subjected to the plate.

	Theoretical value	Coarse grid	Medium grid	Fine grid
Force (N)	941.76	974.47	966.78	957.94
Error $[\varepsilon = (F' - F_0)/F_0]$	–	3.405%	2.665%	1.801%

under the middle grid size. It can be seen that the pressure/stress field is smooth and qualitatively accurate.

The energy conservation property in the whole system of the present coupled method is investigated, referring to the research of Khayyer [35]. In this benchmark test, there is no energy exchange with the surroundings. In a word, the energy of whole system should be conserved, and energy is exclusively exchanged between the fluid and the deformable plate. The energy of the FSI system E_t includes the energy of fluid E_t^F and energy of structure E_t^S. The total energy of the fluid is composed of fluid's kinetic energy E_k^F and fluid's gravitational potential energy E_p^F. The structure's total energy comprises kinetic energy E_k^S, elastic strain energy E_e^S, and gravitational potential energy E_p^S. The formulation of each energy component can be expressed as,

$$E_t = E_t^F + E_t^S \tag{29}$$

$$E_t^F = E_k^F + E_p^F, E_t^S. = E_k^S + E_p^S + E_e^S \tag{30}$$

$$E_k^F = \sum_{i\in\Omega_F} \frac{1}{2} m_i^F |u_i^F|^2, E_p^F = \sum_{i\in\Omega_F} m_i^F \boldsymbol{g}\cdot\boldsymbol{r}_i \tag{31}$$

$$E_k^S = \sum_{i\in\Omega_S} \frac{1}{2} m_i^S |u_i^S|^2, E_p^S = \sum_{i\in\Omega_S} m_i^S \boldsymbol{g}\cdot\boldsymbol{r}_i, E_e^S = \sum_{i\in\Omega_S} \frac{1}{2} \sigma_i^S \boldsymbol{\varepsilon}_i^S V_i \tag{32}$$

The time variations of energy components in the FSI system are presents in Fig. 12. According to Fig. 12(a–e), the kinetic, potential and elastic strain energies of the structure field present oscillation in the initial stage ($t < 0.025$ s), together with the kinetic energy of the fluid field, nevertheless the energy components of the structure field reach almost constant values before $t = 0.2$ s. From Fig. 12(d), the gravitational potential energy of fluid contributes most to the total energy of the flow field and FSI system. There is a slight drop of about 0.02% of the gravitational potential energy, which leads to the drop of about 0.0148% of the total energy of FSI system and normalized total energy of the FSI system ($E_t/E_{t_0} - 1$). The decrease in fluid kinetic energy is not caused by the energy exchange between the structure and the fluid. In general, the coupled method has the properties of energy conservation.

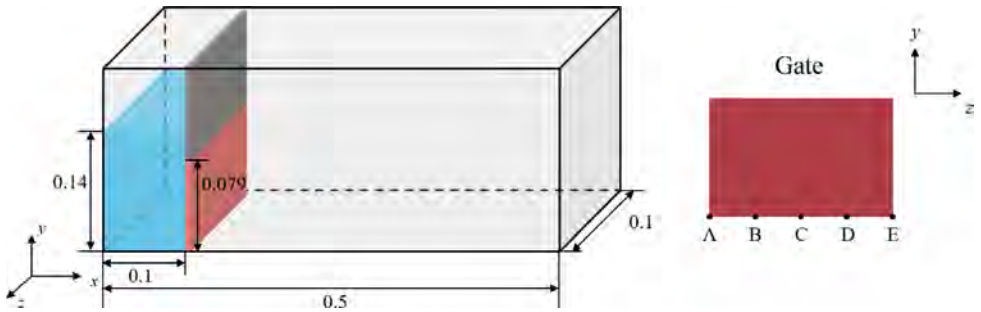

Fig. 19. Schematic view of dam-break flow with the deformable gate.

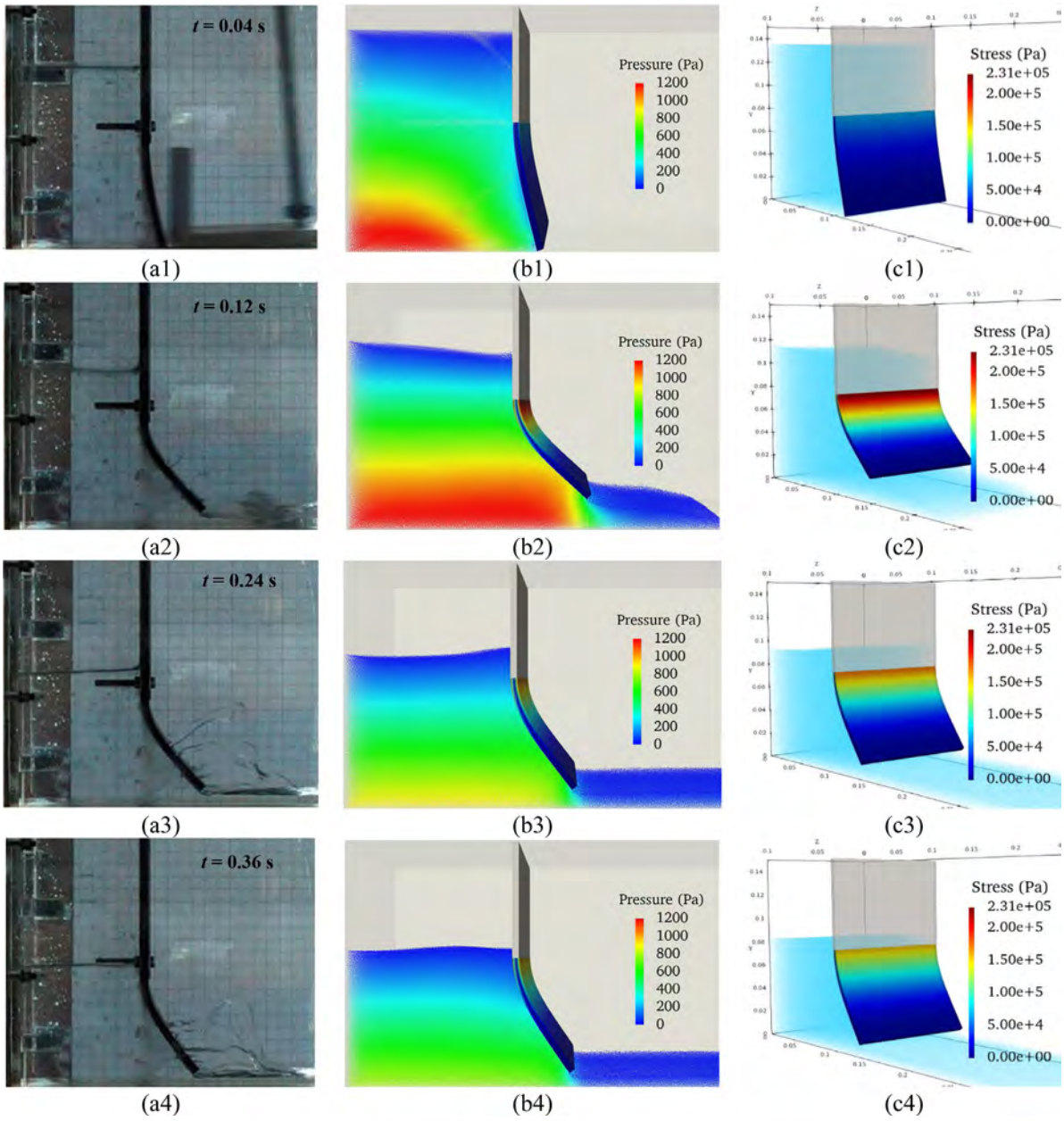

Fig. 20. The dam-break flow interacting with a deformable gate, typical snapshots of (a) the experiment result, (b) the pressure distribution of fluid particle, and (c) the stress distribution of element model.

3.2.2. A 3D forced deformable plate with the initial velocity

The accuracy of the deformation transformation on the interface between the fluid and structure domains is studied in this test. The problem of a forced deformable plate with the initial velocity under the boundary condition of all sides simply supported (SS) is reproduced, the influence of gravity of the plate is not

Table 3
The accuracy analysis of deflection of the plate's mid-point.

	Theoretical value	Coarse grid	Medium grid	Fine grid
Deflection (N)	−1.773E−6	−1.864E−6	−1.828E−6	−1.809E−6
Error $[\varepsilon = (d' - d_0)/\ d_0]$	–	5.132%	3.102%	2.03%

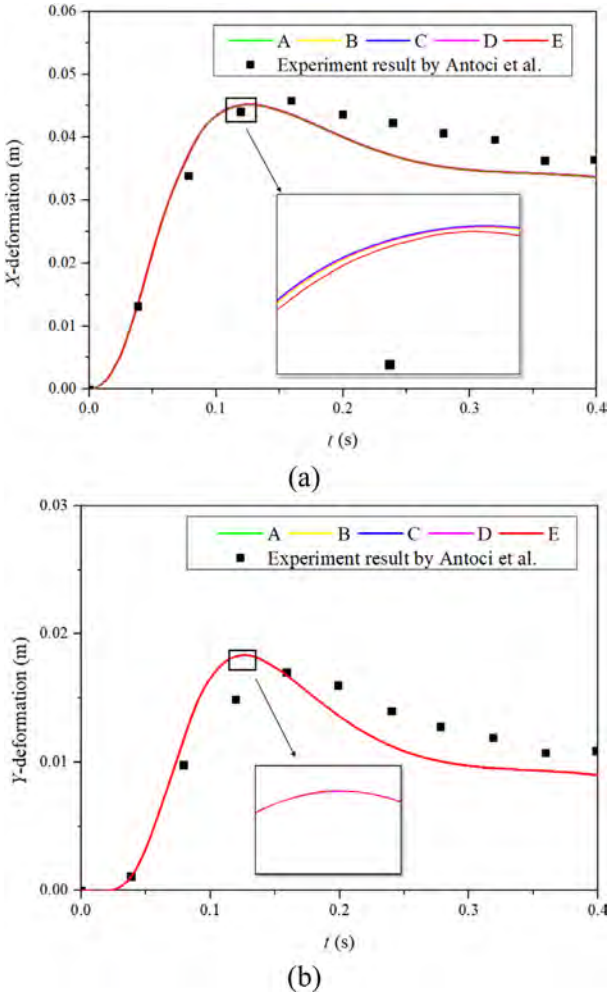

Fig. 21. Horizontal (a) and vertical (b) deformation of free end of the elastic gate.

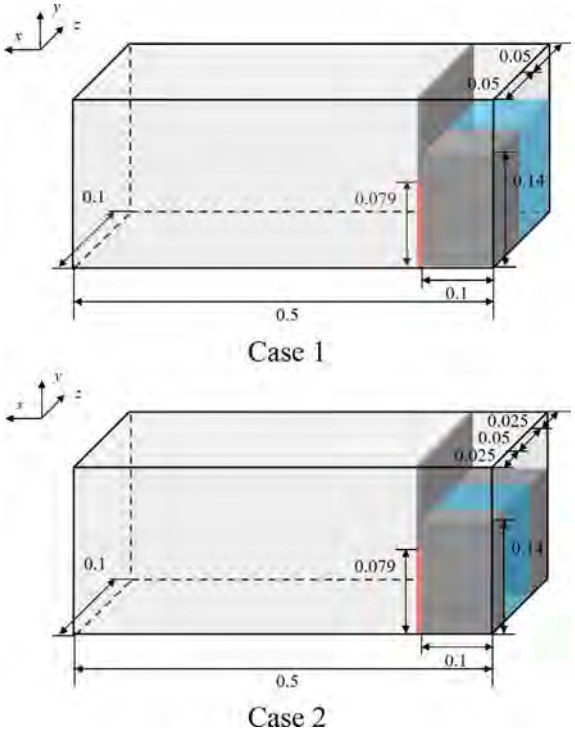

Fig. 22. Schematic view of the narrow dam-break flow with deformable gate, case 1: asymmetrical layout; case 2: symmetrical layout.

taken into account. The thick (h), density (ρ_s), Young's modulus (E_s) and Poisson's ratio (μ_s) of plate are 0.01 m, 1000 kg/m^3, 100 MPa and 0.3, respectively, and the damping effect is considered during the simulation. The initial particle spacing and maximum grid size are set as 0.0025 m and 0.01 m, and the time step is regarded as 0.0005 s. The plate is forced to deform with an initial velocity distribution of $v_y(x, z)$, as follows,

$$v_y = A_{mn} \sin \frac{m\pi x}{a} \cos \frac{n\pi z}{b} \tag{33}$$

where A_{mn} is an amplitude coefficient determined from the initial conditions of the problem, a and b signifies length/width of the square, and m and n are integers denoting governing vibration modes in x and y directions. In this paper, $A_{mn} = 1$, $a = b = 0.4$, $m = 2$ and $n = 2$ will be adopted. The illustration of the computational domain is shown in the Fig. 13.

Through the interfacial data interpolation module, the velocity on the nodes of the element model can be transferred to the particle model. Therefore, the particle model will produce the deformation. For the square plate, the two mode shapes have the same frequency and exist simultaneously, their relative amplitudes depending upon the initial conditions. Because the structural deformation is relatively small, the displacement is magnified in the figure for better observation, with an amplification factor of 25, as demonstrated in Fig. 14. It can be found that the shapes of the two models (the particle model and grid model) are coincident with each other. Fig. 15 compared the structural displacement and particle deformation, the consistency is proved quantitatively. Fig. 16 presents the stress distribution of the element model, it can be noticed that the stress field is smooth, implying the stability of present structure solver. Fig. 17 illuminates the frequency of the vibration of measuring point. It can be found the vibration frequency of plate is 488.96 rad/s. For the analytically vibration frequency, as follows,

$$w = \left[\left(\frac{m\pi}{a}\right)^2 + \left(\frac{n\pi}{b}\right)^2\right]\sqrt{\frac{D}{\rho_s h}} \tag{34}$$

$$D = \frac{E_s h^3}{12(1-\mu^2)} \tag{35}$$

where D presents the bending stiffness of the plate. According to the present result, the frequencies obtained by present method approximates to the analytically value 472.23 rad/s, with the percent deviation ε of 3.54%, where $\varepsilon = {}^{|w_A - w_N|}/_{w_A}$, indicating the accuracy of present method. Fig. 18 exhibits quantitative comparisons the time histories of the structural kinetic energy and the normalized total energy with the theoretical solution. It can be seen that the solver satisfies the characteristic of energy conservation. Despite there is a slight numerical fluctuation in the normalized total energy, which should be a statistical error.

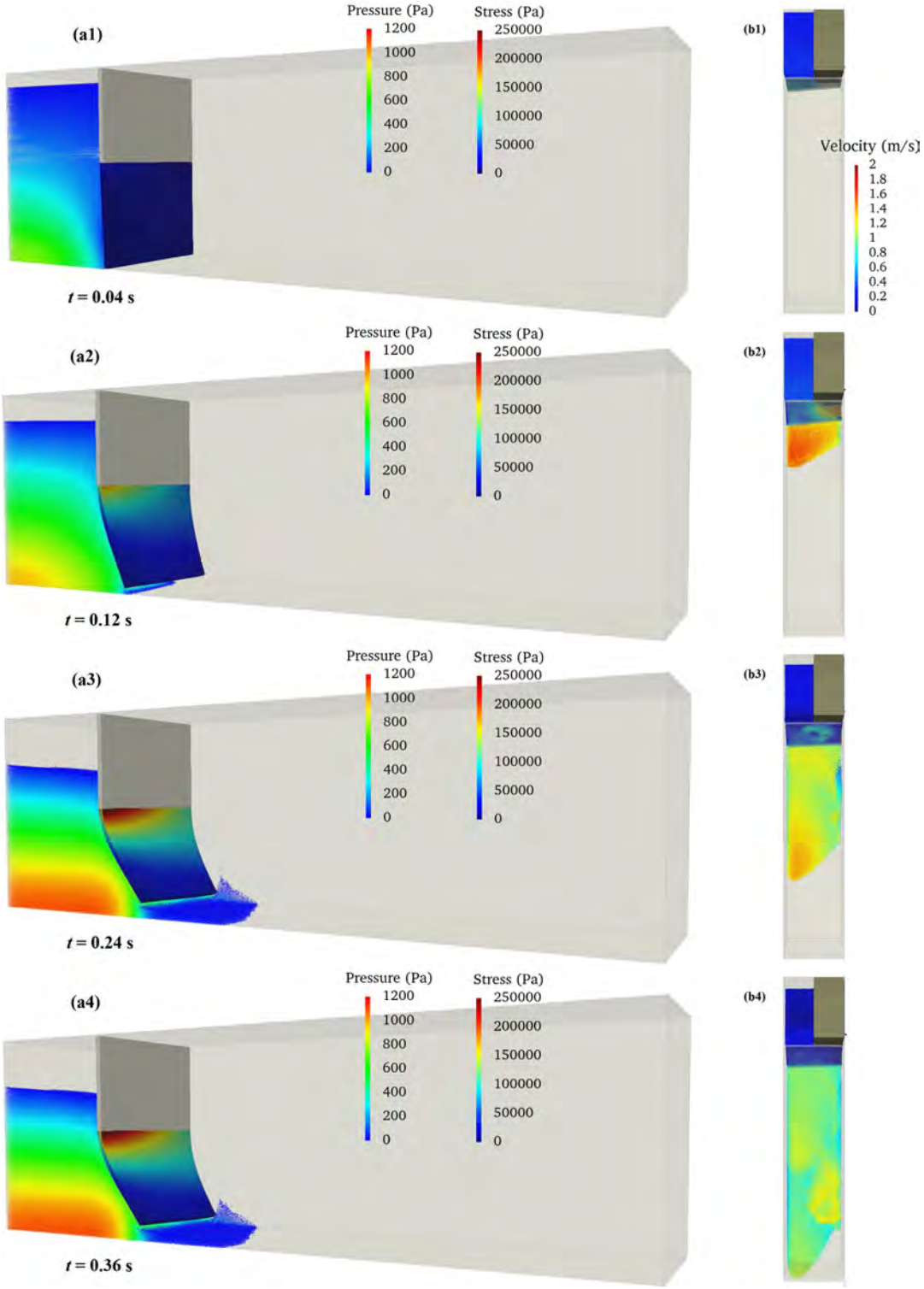

Fig. 23. Typical snapshots of Case 1, (a) the pressure distribution of fluid particle and the stress distribution of element model (b) the velocity of the fluid flow.

Through above two tests, it can be noted that the high-precision interpolation of the force and deformation on the interface can be achieved by proposed data transformation algorithm.

4. Numerical examples

The proposed MPSFSI solver is verified and validated through a classical FSI benchmark test. The test of the dam-break flow with an elastic gate is reproduced and compared with the experiment result [25]. After that, to study the three-dimensional effect, a test of the narrow dam-break flow with an elastic gate with two different layouts is performed. Through the comparison, the structure responses related to the structural safety are investigated.

Table 4
The computational parameters of the case.

Parameters of MPS solver	Value	Parameters of FEM solver	Value
Fluid density (kg/m^3)	1000	Structure density (kg/m^3)	1100
Kinematic viscosity (m^2/s)	1×10^{-6}	Young's modulus (MPa)	10
Particle size (m)	0.00125	Poisson's ratio	0.3
Total particle numbers	1,200,582	Structure dimensions (m $*$ m $*$ m)	0.004 $*$ 0.079 $*$ 0.1
Fluid particle numbers	732,240	Mesh generation	3 $*$ 41 $*$ 16
Time size in fluid domain (s)	1×10^{-4}	Time size in structure domain (s)	1×10^{-4}

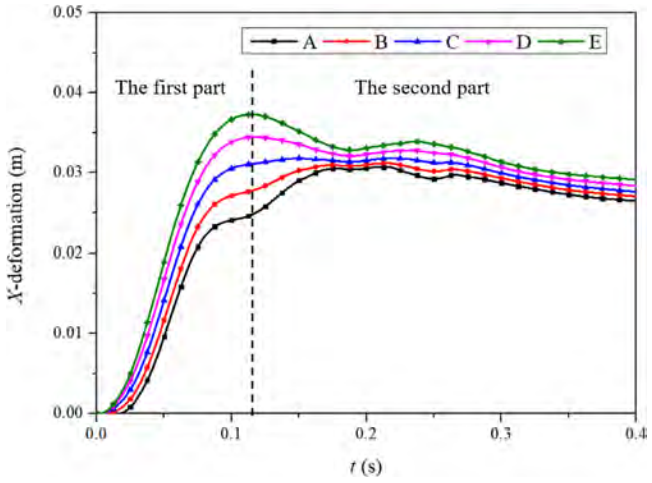

Fig. 24. Horizontal deformation of free end of the elastic gate of Case 1.

4.1. Dam-break flow with an elastic gate

In our previous works, the interaction between two-dimensional dam-break flow and the deformable gate has been numerically simulated [44,56]. Obtained result indicated that the main features of the experimental measurements [25] are generally well reproduced in the simulation. In present paper, the reliability of the MPSFSI solver is tested numerically by simulating the same benchmark problem in the three-dimensional way. The configuration of the system is shown in Fig. 19. A column of water at the left end of the tank is initially in hydrostatic equilibrium state, confined by a gate. The lower part of the gate is a deformable plate. Once the free end of the elastic plate is released, the water pushes away the elastic gate and starts to flow. The dimensions of the test case and the computational parameters are listed in Table 4. Ten-core parallelism is used in CPU computing.

Fig. 20 shows the typical snapshots of numerical results for the free-surface profile and the deformation of the structure compared with the experiment. Once releasing the water column, the gate is forced to deform under the hydrodynamic force of breaking dam, then obvious horizontal displacement can be observed. As the depth of the water flow decreases, the pressure loading on the gate decreases, therefore, the deformable gate gradually returns back to the initial position. The dimension in z-direction of the elastic gate is same as the water column, so that the leakage of water flow between the gate and the wall which is present in the experiments cannot be observed in the simulation. It can be noticed that the dynamic coupling between fluid flow and deformable structure is successfully simulated. Fig. 20 (c1–c4) shows the deformation and stress distribution of the structure. The evolution of the stress distribution is in agreement with the deformation of the structure. It can be observed that the hydrodynamic pressure and structure stress are notable robustness and smoothness by the presented method. However, in spite of the expansion to three-dimensional in this benchmark, obvious three-dimensional effect cannot be observed attributed to consistency in z-direction.

Fig. 21 shows the evolution of the deformation of the elastic gate's free end at different positions (A, B, C, D and E) along the z-direction, compared with the experiment result. The positions of five probes are shown in the Fig. 19. According to the figure, the time-history of deformation obtained by the present method is in good agreement with the experiment data. According to the enlarged figure, a slightly three-dimensional effect can be found. Especially, in the evolution of horizontal deformation, the deflection of middle point (C) is slightly larger than on the sides. Nonetheless, the three-dimensional effect is not obvious in this case. In general, the results show that the present three-dimensional MPS–FEM coupled solver have shown acceptable accuracy and stability in solving FSI problems.

4.2. Narrow dam-break flow with an elastic gate

In the above case, the breadth of dam-break flow is identical with the elastic gate. For the study of three-dimensional effect, the dam-break flow is narrowed to half of the elastic gate in this section. The configuration of the model is exhibited in Fig. 22, two types of different layout are adopted, including asymmetrical arrangement (Case 1) and symmetrical arrangement (Case 2). The physical parameters of fluid and structure domain are the same as the benchmark. The initial particle spacing is 0.00125 m with a total number of about 0.89 million particles, including 0.36 million fluid particles. The simulation physical time is 0.4 s in this case, and the calculation time steps is 0.0001 s. Ten-core parallelism is used in CPU computing.

Fig. 23 shows the typical snapshots of Case 1, the asymmetrical layout. The deformation of the structure, as well as the velocity of the fluid flow can be observed. The lower left of the gate is firstly forced to deform under the hydrodynamic force, a gap between bottom of the gate and right wall is then created. As the deformation of the tip of the gate increases, the water column gradually flows to filling the gap, then the lower right of the gate begins to deform. The dam flows forward and to the right at the same time, the water climbs along the right-side wall. As the depth of the water column decreases, the gate gradually returns back to the initial position. According to the figure, the evolutions of the fluid and structure domain along z-direction behavior quite different in the asymmetrical layout. It can be noticed that strong three-dimensional feature can be observed in this model of narrow dam-break flow with an elastic gate.

Fig. 24 shows the evolution of the horizontal deformation of the elastic gate's free end at different positions (A, B, C, D and E) along the z-direction, the positions of five probes are same as previous section (Fig. 19). In the first part, the deformation increases rapidly, the deformation of probe located in the side of water column is much larger than the wall side. In the second part, the deflections of all points gradually fall back towards the initial position, and close to each other. From the figure, an obvious three-dimensional feature of the evolution of the structural deflection can be found, which is in agreement with the conclusion we got according to Fig. 23.

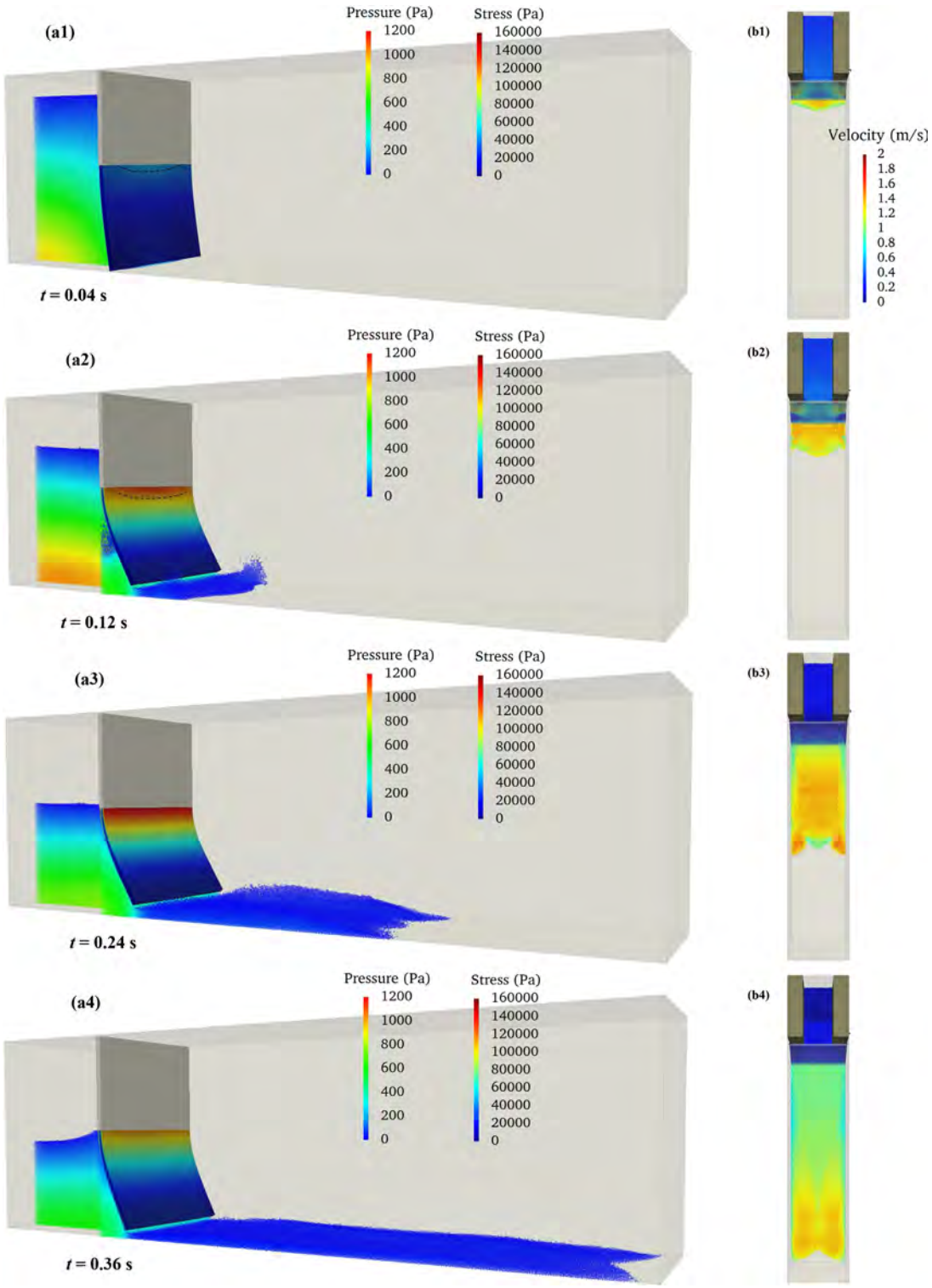

Fig. 25. Typical snapshots of Case 2, (a) the pressure distribution of fluid particle and the stress distribution of element model (b) the velocity of the fluid flow.

Fig. 25 presents the typical snapshots of Case 2, the symmetrical layout. Different from the asymmetrical layout (Case 1), the water flows from the lower middle of the gate in the beginning, the lower middle of the gate presents the deformation. The stress distribution on the structure model is radiating from the middle of the gate. Then, as the water column gradually flows to filling the gap between the wall and the deformable gate, the stress distribution on the element model is uniform along the z-direction. According to Fig. 25 (b), the water flow spills out from the middle first, a distinct water head in the middle. Then, as the water flows to both sides, and creates water climbing phenomenon. Meanwhile, there are three obvious water heads, moreover, the speed of water heads on both sides is faster than that of the middle water head. In the end, the water heads of both two sides gradually squeeze towards the middle and collide to form a splash, therefore, there are only two sides water heads existing. The streamline of dam-break flow at time points of 0.24 and 0.36 s in Fig. 26 can be more apparently demonstrated

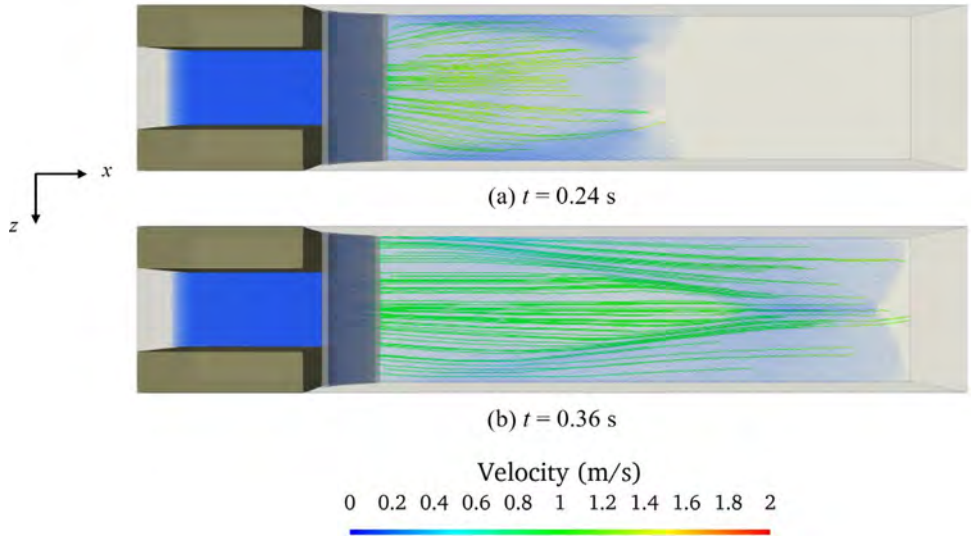

Fig. 26. The streamline of dam-break flow at time points of 0.24 and 0.36 s.

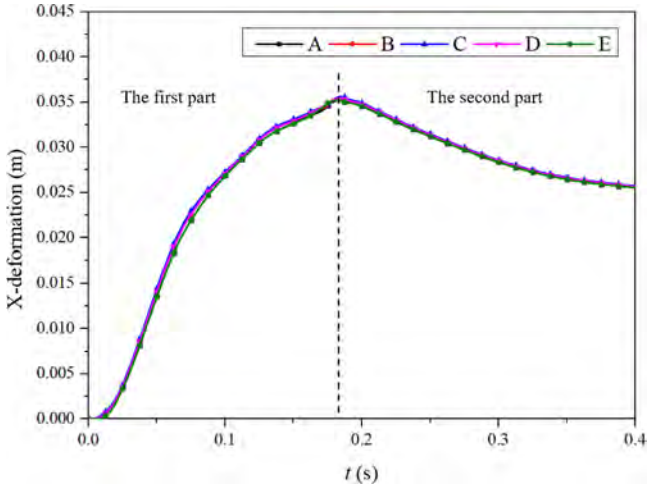

Fig. 27. Horizontal deformation of free end of the elastic gate of Case 2.

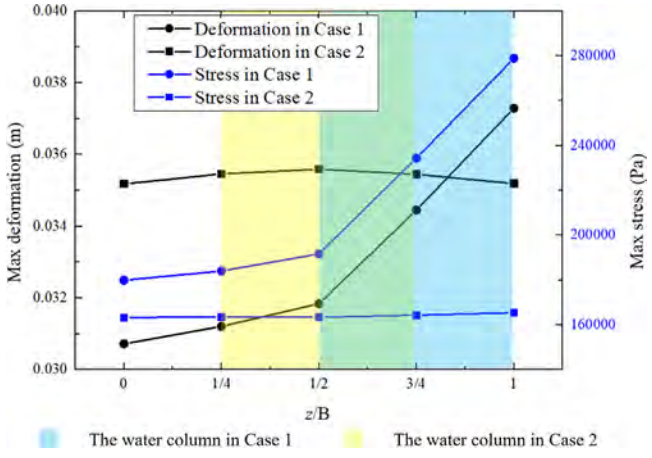

Fig. 28. The deformation and stress distribution along the z-direction of two cases.

the phenomenon. According to the figure, the water head and the fluid velocity are nonuniform and symmetrical along the z-direction, however, the stress on the element model presents approximately uniform distribution. It can be noticed that strong three-dimensional feature in fluid domain can be observed in this model, nonetheless, not in structure domain.

Fig. 27 shows the evolution of the deformation of the elastic gate's free end at different points (A, B, C, D and E) along the z-direction, the positions of five probes are same as previous section (Fig. 19). According to the figure, in the first part, the deformations of all points increase gradually, and the deformation of middle point C is slightly larger than the others and the deformations of point A and E are slightly smaller. In the second part, all points' deformations decrease gradually, with no obvious three-dimensional effect.

The structure response in above two cases, asymmetrical and symmetrical layout, are compared in Fig. 28, where the maximum displacement and maximum stress of five equal interval cross sections are displayed. According to the figure, strong three-dimensional phenomenon can be observed in Case 1, which is not obvious in Case 2. The deformation of each section in Case 1 tends to increase along the z-direction, and on the side of water column, the increase is dramatic. However, the deformation in Case 2 is smooth, there is no clear increase within the range of the water column. The stress distributions of both two case are consistent with their deformation trend. In the view of the structural response, the average displacement of Case 2 is larger, while the local displacement of Case 1 is relatively distinct as well as the stress distribution, which is more challenging to the structural strength and stability.

In the view of the energy transformation, the two layouts have the same energy at the initial status. Fig. 29 presents time histories of structural energy components in the FSI system under two layouts. From Fig. 29(d), it can be found that the structural total energy obtained through the FSI system in both configurations is ultimately close. In the asymmetrical arrangement, the energy of the deformable gate increases rapidly in the initial stage, followed by a period of fluctuation. In the symmetrical arrangement, the energy of the deformable gate tends to increase first and then decrease. In the symmetrical arrangement, the instantaneous energy obtained by the structure is larger than the asymmetrical one.

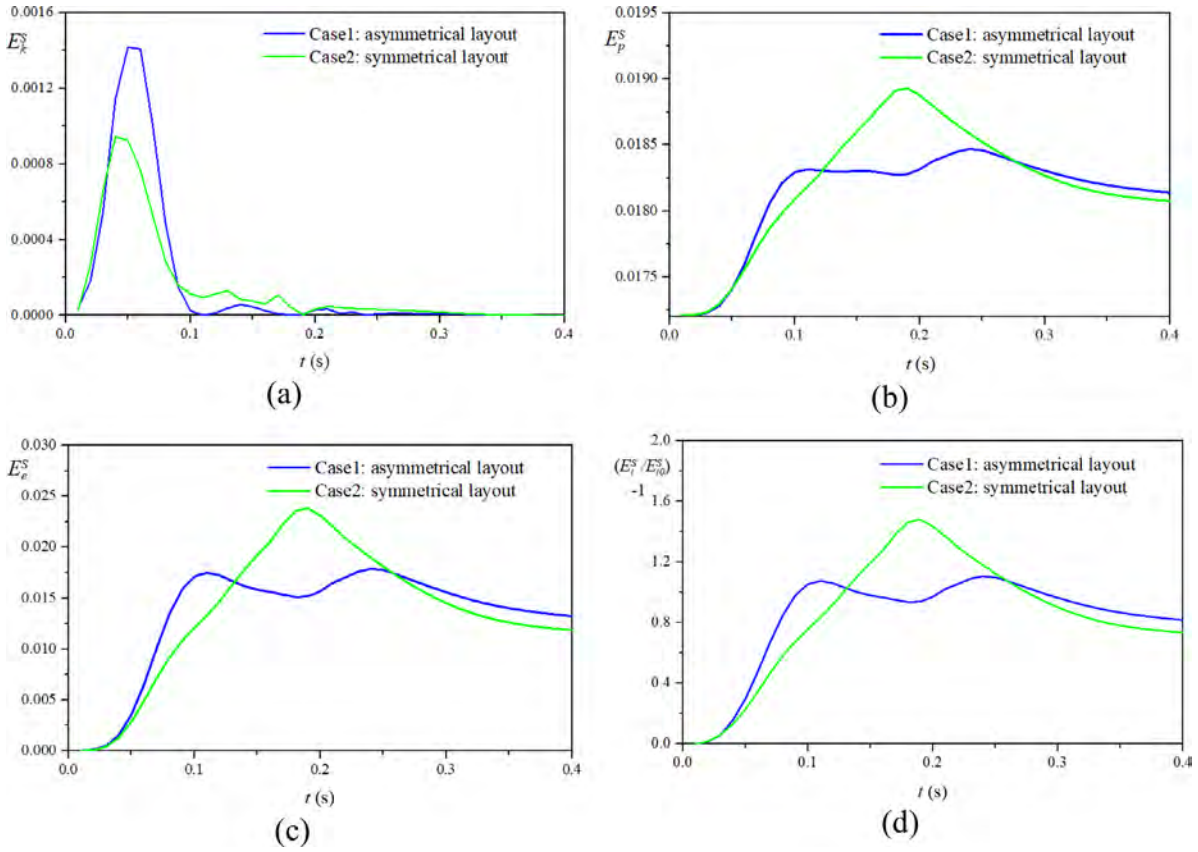

Fig. 29. Time histories of structural energy components under two layouts, (a) kinetic energy of structure, (b) gravitational potential energy of structure, (c) elastic strain energy of structure, (d) normalized total energy of structure.

5. Conclusions

The MPS–FEM coupled method is developed for 3D FSI problems. In the proposed method, the fluid field is solved by Moving Particle Semi-implicit (MPS) method, while the solid part is modeled with FEM. A partitioned coupling strategy of traditional Conventional Serial Staggered (CSS) strategy is employed for MPS method and FEM method coupling. On the fluid–structure interface, an interpolation technique, called 3D-KFBI, is adopted for force and deformation interpolation. The accuracy of interpolation modules is validated by two numerical tests, including a hydrostatic water column on a deformable plate and a forced plate with an initial velocity. The conservation of the force and deformation in the interface can be achieved. In addition, the energy conservation property of the present MPS–FEM coupled solver is proved.

After that, the FSI benchmark test of dam-break flow through an elastic gate is performed as the validation of proposed method. The obtained numerical result is in good agreement with experiment result, which can indicate that the present method has high-accuracy and strong robustness. Moreover, simulations of narrow dam-break flow with an elastic gate are carried out to investigate the three-dimensional feature. Strong three-dimensional phenomenon of fluid field can be observed in both symmetrical and symmetrical layouts. However, three-dimensional feature of structure field can only be clearly noticed in asymmetrical layout. In general, the outcome indicates that the present solver can be used to solve 3D FSI problems. Our approach presents the potential to be widely used in FSI problems. In the future, the proposed method will be applied in more complicated and practical FSI problems.

Declaration of competing interest

The authors declare the following financial interests/personal relationships which may be considered as potential competing interests: Decheng Wan reports financial support was provided by Shanghai Jiao Tong University.

Data availability

The data that support the findings of this study are available from the corresponding author upon reasonable request.

Acknowledgments

This work was supported by National Natural Science Foundation of China (Grant No. 51879159, 52131102), National Key Research and Development Program of China (2019YFB1704200), to which the authors are most grateful.

References

[1] E. Oñate, S.R. Idelsohn, F. Del Pin, R. Aubry, The particle finite element method. An overview, Int. J. Comput. Method 2 (2004) 267–307.
[2] S.R. Idelsohn, E. Oñate, F. Del Pin, N. Calvo, Fluid–structure interaction using the particle finite element method, Comput. Methods Appl. Mech. Engrg. 195 (2006) 2100–2123.
[3] S.R. Idelsohn, J. Marti, A. Souto-Iglesias, E. Oñate, Interaction between an elastic structure and free-surface flows: experimental versus numerical comparisons using the PFEM, Comput. Mech. 43 (1) (2008) 125–132.
[4] E. Oñate, M.A. Celigueta, S.R. Idelsohn, F. Salazar, B. Suárez, Possibilities of the particle finite element method for fluid–soil–structure interaction problems, Comput. Mech. 48 (3) (2011) 307.

[5] K.P. Liao, C.H. Hu, A coupled FDM-FEM method for free surface flow interaction with thin elastic plate, J. Mar. Sci. Technol. 18 (1) (2013) 1–11.
[6] K.P. Liao, C.H. Hu, M. Sueyoshi, Free surface flow impacting on an elastic structure: experiment versus numerical simulation, Appl. Ocean Res. 50 (2015) 192–208.
[7] K.J. Paik, P.M. Carrica, Fluid–structure interaction for an elastic structure interacting with free surface in a rolling tank, Ocean Eng. 84 (2014) 201–212.
[8] Q. Qu, W. Rui, G. Hao, P. Liu, R.K. Agarwal, Numerical study of water impact of an elastic cylindrical shell using coupled FVM-FEM method, in: 54th AIAA Aerospace Sciences Meeting, 2006.
[9] L.B. Lucy, A numerical approach to the testing of the fission hypothesis, Astron. J. 82 (1977) 1013–1024.
[10] S. Koshizuka, Y. Oka, Moving-particle semi-implicit method for fragmentation of incompressible fluid, Nucl. Sci. Eng. 123 (3) (1996) 421–434.
[11] M. Gomez-Gesteira, R.A. Dalrymple, Using a three-dimensional smoothed particle hydrodynamics method for wave impact on a tall structure, J. Waterw. Port Coast. Ocean Eng. 130 (2) (2004) 63–69.
[12] Z.Y. Tang, Y.L. Zhang, D.C. Wan, Multi-resolution MPS method for free surface flows, Int. J. Comput. Methods 13 (4) (2016) 1–17.
[13] X. Chen, D.C. Wan, GPU accelerated MPS method for large-scale 3-D violent free surface flows, Ocean Eng. 171 (2019) 677–694.
[14] K. Gong, H. Liu, B.L. Wang, Water entry of a wedge based on SPH model with an improved boundary treatment, J. Hydrodyn. 21 (6) (2009) 750–757.
[15] G. Oger, D.L. Touzé, B. Alessandrini, P. Maruweski, A new parallelized 3d sph model: resolution of water entry problems and scalability study, Ercoftac Bull. 76 (1) (2008) 145–149.
[16] P.N. Sun, F.R. Ming, A.M. Zhang, Numerical simulation of interactions between free surface and rigid body using a robust SPH method, Ocean Eng. 98 (2015) 32–49.
[17] B.H. Lee, S.M. Jeong, S.C. Hwang, J.C. Park, M.H. Kim, A particle simulation of 2-D vessel motions interacting with liquid-sloshing cargo, Comput. Model. Eng. Sci. 91 (1) (2013) 43–63.
[18] Y.X. Zhang, D.C. Wan, Comparative study of MPS method and level-set method for sloshing flows, J. Hydrodyn. 26 (4) (2014) 577–585.
[19] H.Z. Li, Z.Y. Tang, D.C. Wan, Application of GPU acceleration techniques in 3D violent free surface flows, Ocean Eng. 34 (5) (2016) 20–29, in Chinese.
[20] F.Z. Xie, W.W. Zhao, D.C. Wan, CFD simulations of three-dimensional violent sloshing flows in tanks based on MPS and GPU, J. Hydrodyn. 32 (5) (2020) 672–683.
[21] M. Sueyoshi, M. Kashiwagi, S. Naito, Numerical simulation of wave-induced nonlinear motions of a two-dimensional floating body by the moving particle semi-implicit method, J. Mar. Sci. Technol. 13 (2) (2008) 85–94.
[22] K. Shibata, S. Koshizuka, M. Sakai, K. Tanizawa, Lagrangian simulations of ship wave interactions in rough seas, Ocean Eng. 42 (2012) 13–25.
[23] K. Guo, P.N. Sun, X.Y. Cao, X. Huang, A 3-D SPH model for simulating water flooding of a damaged floating structure, J. Hydrodyn. 29 (5) (2017) 831–844.
[24] B.Y. Ni, D.F. Han, S.C. Di, Y.Z. Xue, On the development of ice-water-structure interaction, J. Hydrodyn. 32 (18) (2020).
[25] Y. Zhu, C. Zhang, Y. Yu, X. Hu, A CAD-compatible body-fitted particle generator for arbitrarily complex geometry and its application to wave-structure interaction, J. Hydrodyn. 33 (2) (2021) 195–206.
[26] X. Wen, W.W. Zhao, D.C. Wan, An improved moving particle semi-implicit method for interfacial flows, Appl. Ocean Res. 117 (2021) 102963.
[27] E. Harada, H. Ikari, T. Tazaki, H. Gotoh, Numerical simulation for coastal morphodynamics using DEM-MPS method, Appl. Ocean Res. 117 (2021) 102905.
[28] F.Z. Xie, W.W. Zhao, D.C. Wan, Numerical simulations of liquid–solid flows with free surface by coupling IMPS and DEM, Appl. Ocean Res. 117 (2021) 102771.
[29] H. Gotoh, A. Khayyer, Y. Shimizu, Entirely Lagrangian meshfree computational methods for hydroelastic fluid–structure interactions in ocean engineering—Reliability, adaptivity and generality, Appl. Ocean Res. 115 (2021) 102822.
[30] C. Antoci, M. Gallati, S. Sibilla, Numerical simulation of fluid–structure interaction by SPH, Comput. Struct. 85 (11) (2007) 879–890.
[31] M.B. Liu, J.R. Shao, H.Q. Li, Numerical simulation of hydro-elastic problems with smoothed particle hydrodynamics method, J. Hydrodyn. 25 (5) (2013) 673–682.
[32] S.C. Hwang, A. Khayyer, H. Gotoh, J.C. Park, Development of a fully Lagrangian MPS-based coupled method for simulation of fluid–structure interaction problems, J. Fluids Struct. 50 (2014) 497–511.
[33] S.C. Hwang, J.C. Park, H. Gotoh, A. Khayyer, K.J. Kang, Numerical simulations of sloshing flows with elastic baffles by using a particle-based fluid–structure interaction analysis method, Ocean Eng. 118 (2016) 227–241.
[34] C. Yang, H.X. Zhang, Numerical simulation of the interactions between fluid and structure in application of the MPS method assisted with the large eddy simulation method, Ocean Eng. 155 (2018) 55–64.
[35] A. Khayyer, H. Gotoh, H. Falahaty, Y. Shimizu, An enhanced ISPH-SPH coupled method for simulation of incompressible fluid-elastic structure interactions, Comput. Phys. Commun. 232 (2018) 139–164.
[36] H. Falahaty, A. Khayyer, H. Gotoh, Enhanced particle method with stress point integration for simulation of incompressible fluid-nonlinear elastic structure interaction, J. Fluids Struct. 81 (2018) 325–360.
[37] A. Khayyer, N. Tsuruta, Y. Shimizu, H. Gotoh, Multi-resolution MPS for incompressible fluid-elastic structure interactions in ocean engineering, Appl. Ocean Res. 82 (2019) 397–414.
[38] H.G. Lyu, P.N. Sun, T. Xiao, S.H.C. Huang, A.M. Zhang, On removing the numerical instability induced by negative pressures in SPH simulations of typical fluid–structure interaction problems in ocean engineering, Appl. Ocean Res. 114 (2021) 102938.
[39] A. Khayyer, H. Gotoh, Y. Shimizu, Y. Nishijima, A 3D Lagrangian mesh-free projection-based solver for hydroelastic fluid-structure interactions, J. Fluids Struct. 105 (2021) 103342.
[40] P.N. Sun, D.L. Touzé, G. Oger, An accurate FSI-SPH modeling of challenging fluid–structure interaction problems in two and three dimensions, Ocean Eng. 221 (2021) 108552.
[41] A. Yilmaz, S. Kocaman, M. Demirci, Numerical analysis of hydroelasticity problems by coupling WCSPH with multibody dynamics, Ocean Eng. 25 (2021) 110205.
[42] Z. Sun, K. Djidjeli, J.T. Xing, F. Cheng, Coupled MPS-modal superposition method for 2D nonlinear fluid–structure interaction problems with free surface, J. Fluids Struct. 61 (2016) 295–323.
[43] Z. Sun, G.Y. Zhang, Z. Zong, K. Djidjeli, J.T. Xing, Numerical analysis of violent hydroelastic problems based on a mixed MPS-mode superposition method, Ocean Eng. 179 (2019) 285–297.
[44] C.J.K. Lee, H. Noguchi, S. Koshizuka, Fluid–shell structure interaction analysis by coupled particle and finite element method, Comput. Struct. 85 (11) (2007) 688–697.
[45] N. Mitsume, S. Yoshimura, K. Murotani, T. Yamada, MPS-FEM partitioned coupling approach for fluid–structure interaction with free surface flow, Int. J. Comput. Methods 11 (4) (2014) 4157–4160.
[46] N. Mitsume, S. Yoshimura, K. Murotani, T. Yamada, Improved MPS-FE fluid-structure interaction coupled method with MPS polygon wall boundary model, Comput. Model. Eng. Sci. 101 (4) (2014) 229–247.
[47] Z.M. Zheng, G.T. Duan, N. Mitsume, S.H. Chen, S. Yoshimura, A novel ghost cell boundary model for the explicit moving particle simulation method in two dimensions, Comput. Mech. 66 (4) (2020) 87–102.
[48] Z.M. Zheng, G.T. Duan, N. Mitsume, S.H. Chen, S. Yoshimura, An explicit MPS/FEM coupling algorithm for three-dimensional fluid–structure interaction analysis, Eng. Anal. Bound. Elem. 121 (2020) 192–206.
[49] G.Y. Zhang, W.W. Zhao, D.C. Wan, Partitioned MPS-FEM method for free-surface flows interacting with deformable structures, Appl. Ocean Res. 114 (2021) 102775.
[50] G. Fourey, G. Oger, D.L. Touzé, B. Alessandrini, Violent fluid-structure interaction simulations using a coupled SPH/FEM method, in: Iop Conference Series Materials Science & Engineering, Vol. 10, 2010, 012041.
[51] G. Fourey, C. Hermange, D.L. Touzé, G. Oger, An efficient FSI coupling strategy between smoothed particle hydrodynamics and finite element methods, Comput. Phys. Commun. 217 (2017) 66–81.
[52] Q. Yang, V. Jones, L. McCue, Free-surface flow interactions with deformable structures using an SPH-FEM model, Ocean Eng. 55 (2012) 136–147.
[53] C. Hermange, G. Oger, D.L. Touzé, Energy considerations in the SPH method with deformable boundaries and application to FSI problems, J. Comput. Phys. X1 (2019) 100008.
[54] Z.L. Zhang, M.S.U. Khalid, T. Long, M.B. Liu, C. Shu, Improved element-particle coupling strategy with δ-SPH and particle shifting for modeling sloshing with rigid or deformable structures, Appl. Ocean Res. 114 (2021) 102774.
[55] Y.L. Zhang, D.C. Wan, MPS-FEM coupled method for sloshing flows in an elastic tank, Ocean Eng. 152 (2018) 416–427.
[56] C. Hermange, G. Oger, Y.L. Chenadec, D.L. Touzé, A 3D SPH–FE coupling for FSI problems and its application to tire hydroplaning simulations on rough ground, Comput. Methods Appl. Mech. Engrg. 355 (2019) 558–590.
[57] S. Lee, J.W. Hong, Parametric studies on smoothed particle hydrodynamic simulations for accurate estimation of open surface flow force, Int. J. Nav. Archit. Ocean Eng. 12 (2020) 85–101.
[58] Y.X. Zhang, D.C. Wan, Apply MPS method to simulate liquid sloshing in LNG tank, in: Proceedings of 22nd International Offshore and Polar Engineering Conference. June 17-23 (2012), pp. 381–391.
[59] Z.Y. Tang, D.C. Wan, Numerical simulation of impinging jet flows by modified MPS method, Eng. Comput. 32 (4) (2015) 1153–1171.
[60] Z.Y. Tang, Y.L. Zhang, D.C. Wan, Multi-resolution MPS method for free surface flows, Int. J. Comput. Methods 13 (4) (2016) 1641018-1-1641018-17.

[61] Y.L. Zhang, X. Chen, D.C. Wan, An MPS-FEM coupled method for the comparative study of liquid sloshing flows interacting with rigid and elastic baffles, Appl. Math. Mech. 37 (12) (2016) 1359–1377.
[62] Y.L. Zhang, D.C. Wan, Numerical study of interactions between waves and free rolling body by IMPS method, Comput. Fluids 155 (2017) 124–133.
[63] C.P. Rao, D.C. Wan, Numerical study of the wave-induced slamming force on the elastic plate based on MPS-FEM coupled method, J. Hydrodyn. 30 (1) (2018) 70–78.
[64] G.Y. Zhang, X. Chen, D.C. Wan, MPS-FEM coupled method for study of wave-structure interaction, J. Mar. Sci. Appl. 18 (4) (2019) 387–399.
[65] M. Tanaka, T. Masunaga, Stabilization and smoothing of pressure in MPS method by quasi-compressibility, J. Comput. Phys. 229 (11) (2010) 4279–4290.
[66] B.H. Lee, J.C. Park, M.H. Kim, S.C. Hwang, Step-by-step improvement of mps method in simulating violent free-surface motions and impact-loads, Comput. Methods Appl. Mech. Engrg. 200 (9–12) (2011) 1113–1125.
[67] A. Khayyer, H. Gotoh, S.D. Shao, Enhanced predictions of wave impact pressure by improved incompressible SPH methods, Appl. Ocean Res. 31 (2) (2009) 111–131.
[68] N.M. Newmark, A method of computation for structural dynamics, J. Eng. Mech. Div. 85 (3) (1959) 67–94.
[69] K.M. Hsiao, J.Y. Lin, W.Y. Lin, A consistent corotational finite element formulation for geometrically nonlinear dynamic analysis of 3-D beams, Comput. Methods Appl. Mech. Engrg. 169 (1999) 1–18.
[70] A.C. Ugural, Stresses in Beams, Plates, and Shells, third ed., in: Applied and Computational Mechanics, CRC Press, Boca Raton, ISBN: 978-1439802700, 2009.